UNIVERSITY OF SCIENCE AND TECHNOLOGY OF HANOI

Department of Space and Earth Sciences

FINAL REPORT

BACHELOR GRADUATION

By:

Pham Phuong Anh

Project:

*

STUDY OF THE CORRELATION BETWEEN HIGH-ENERGY MUONS AND NEUTRINOS IN EXTENSIVE AIR SHOWERS AT ICECUBE OBSERVATION LEVEL

*

Supervisors: *Dr. Son Cao (IFIRSE, ICISE)*
Dr. Donghwa Kang (IAP, KIT)
Dr. Andreas Haungs (IAP, KIT)

Jul 12, 2026

UNIVERSITY OF SCIENCE AND TECHNOLOGY OF HANOI
Department of Space and Earth Sciences

Study of the correlation between high-energy muons and neutrinos in extensive air showers at IceCube observation level

Final Internship Report submitted in partial fulfillment of the requirements for the Bachelor's degree

Student:	Pham Phuong Anh
Student ID:	23BI14054
Major:	Space Science and Satellite Technology
Intake year:	2023
Academic year:	2026

Supervisor 1:	Dr. Son Cao
Affiliation:	IFIRSE, ICISE
Supervisor 2:	Dr. Donghwa Kang
Affiliation:	IAP, KIT
Supervisor 3:	Dr. Andreas Haungs
Affiliation:	IAP, KIT

Quy Nhon, 2026

Contents

Acknowledgements

To be able to finish this thesis, I owe my sincere gratitude to many people. First and foremost, I would like to express my deepest appreciation to my supervisors, Dr. Son Cao, Dr. Donghwa Kang, and Dr. Andreas Haungs. Dr. Son Cao's working philosophy of embracing curiosity and education with kindness has created an inspiring learning environment for young students who just get one foot wet in science research, like me. I am deeply grateful for his patience with my rawness and for his encouragement and support, not only throughout this thesis but also during my previous experiences in his lab, that has broadened my horizon of insight into scientific research and collaboration, and taught me what it means to become a good scientist.

This thesis would not have been possible without the support of Dr. Andreas Haungs and Dr. Donghwa Kang and their research group at the Institute of Astroparticle Physics at KIT, Germany. Despite the unfortunate circumstances that prevented me from joining their project as originally planned, they agreed to support me remotely through a newly proposed project that could be carried out in collaboration with the neutrino group in Vietnam. I am deeply grateful for their kind and thoughtful gesture. I would especially like to thank Dr. Donghwa Kang for her remarkable support despite the distance, the time difference, her busy schedule, and also, at times, the severe heatwave in Germany. She always found time to check on my progress each week and carefully read every line of my thesis draft. Her attention and professional advice contributed tremendously to this work. The kindness of Dr Andreas Haungs and Dr Donghwa Kang has motivated me to get to continue working with them in the future, or, at the very least, to visit them one day in Karlsruhe and finally give them the Vietnamese treats I had prepared.

During my three months working on this project in Quy Nhon, I would also like to thank every member of the neutrino group, who made my journey not only easier but also packed with fun and a lot of good meals. I extend a special thank-you to my lab brother, Sang, for his friendship and generous help with everything from finding accommodation to becoming my "personal chauffeur" around the beautiful city of Quy Nhon. I would also like to thank the President, Vice-President, and all the staff members at the ICISE centre for their work and support for the interns here. And as perhaps the biggest dog person in the universe, I must also thank the dogs at ICISE for their companionship, especially Lu, the smartest, most joyful, and best-behaved dog, who reminded me of my own late dog, Micky.

I am also owe my appreciation to the people in my department at USTH. I would like to thank all the professors and Ms Tra for their enthusiastic support for the students and their study journey at USTH. I am especially thankful to my friends, the "Super Sentai" gang of five, for their companionship, endless silly conversations, and constant support. Special thanks also go to my social brothers, Trong and Huy, for their advice and unwavering support throughout my academic journey. My gratitude extends to everyone, named or unnamed, whose path has crossed mine or who continues to accompany me. Each of you has contributed in some way to shaping the person I am today.

And lastly, to my beloved mum: I owe you all the time, hard work, and joy of your life that you have transformed into me. You have given me everything I have needed and even many things I have unreasonably demanded, while still giving me the freedom and space to grow anyhow as I seek. Your love and endless support are beyond words. They will remain forever engraved in my heart and mind and will be part of everything I am, everything I achieve, and everything I may one day become.

"I can feel the limits of what humans are capable of - that a certain type of perfection can only be realized through a limitless accumulation of the imperfect."

—Haruki Murakami, Kafka on the Shore

List of Abbreviations

CR	Cosmic Rays
EAS	Extensive Air Showers
MC	Monte Carlo
CORSIKA	COsmic Ray SImulations for KAscade
MCEq	Matrix Cascade Equations
FLUKA	FLUctuating KAscade
PEANUT	Pre-Equilibrium Approach to Nuclear Thermalisation
GINC	Generalised Intra-Nuclear Cascade
LPM	Landau-Pomeranchuk-Migdal

Abstract

This thesis investigates the correlation between conventional atmospheric muons and neutrinos in extensive air showers at the IceCube observation level, using CORSIKA simulations of proton- and iron-induced showers over primary energies from 10^{14} to $10^{15.9}$ eV. The CORSIKA average lepton spectra were benchmarked against MCEq calculations under the same physical configurations for the first time. The results showed good overall agreement, the small differences are under discussion. Pearson correlation heatmaps and linear fits indicate that muon multiplicities are more strongly correlated with muon-neutrino multiplicities than with electron-neutrino multiplicities, consistent with their common production in the hadronic cascade. The strongest correlated secondary-energy bins differ between proton and iron showers over different primary energies, demonstrating the influence of primary mass and its energy on shower development. These results show that muon-neutrino correlations provide useful information for future air-shower simulation and possible hadronic interaction models classification studies.

Keywords: cosmic rays, extensive air showers, CORSIKA 7, MCEq, atmospheric muons, atmospheric neutrinos, IceCube

***

Tóm tắt

Luận văn này nghiên cứu mối tương quan giữa các hạt muon và neutrino khí quyển thông thường (conventional atmospheric muon, neutrino) trong các trận mưa hạt khí quyển mở rộng (extensive air showers) tại độ sâu quan sát của IceCube, sử dụng các mô phỏng CORSIKA cho trận mưa hạt sinh bởi proton và hạt nhân sắt với năng lượng sơ cấp từ 10^{14} đến $10^{15.9}$ eV. Phổ lepton trung bình từ CORSIKA lần đầu tiên được đối chiếu (benchmark) với các kết quả tính toán bằng MCEq trong cùng một cấu hình vật lý. Kết quả cho thấy sự tương đồng tổng thể tốt, trong khi các khác biệt nhỏ đang được xem xét và thảo luận. Các bản đồ nhiệt tương quan Pearson và các mô hình hồi quy tuyến tính chỉ ra rằng số lượng hạt muon có tương quan mạnh hơn với số lượng hạt muon-neutrino so với số lượng hạt electron-neutrino; điều này phù hợp với cơ chế sinh ra chúng trong quá trình thác đổ hadron (hadronic cascade). Các khoảng năng lượng của hạt thứ cấp (secondary-energy bin) mà có độ tương quan muon-neutrino mạnh nhất thay đổi tùy theo loại hạt sơ cấp (proton hay sắt) và mức năng lượng sơ cấp, qua đó thể hiện ảnh hưởng của khối lượng và năng lượng của hạt sơ cấp đối với sự phát triển của trận mưa hạt. Những kết quả này cho thấy mối tương quan muon-neutrino cung cấp thông tin hữu ích cho các nghiên cứu mô phỏng mưa hạt cũng như các nghiên cứu tiềm năng về phân loại mô hình tương tác hadron trong tương lai.

Từ khóa: tia vũ trụ, mưa hạt khí quyển, CORSIKA 7, MCEq, muon khí quyển, neutrino khí quyển, IceCube

Chapter 1

Introduction

1.1 Global context

High-energy cosmic-ray research aims to determine the energy spectrum, mass composition, and arrival-direction anisotropy of primary particles (Kang and Haungs, 2024). These observables provide essential information about the origin and propagation of cosmic rays. Because high-energy cosmic rays are rare, direct balloon and satellite measurements lose statistical significance above about $10^{14} - 10^{15}$ eV, cosmic rays above this energy range must be studied indirectly through extensive air showers with detectors on the ground. These air-shower measurements are also relevant for neutrino astronomy, because the primary cosmic-ray spectrum and mass composition are required inputs for determining the atmospheric neutrino flux.

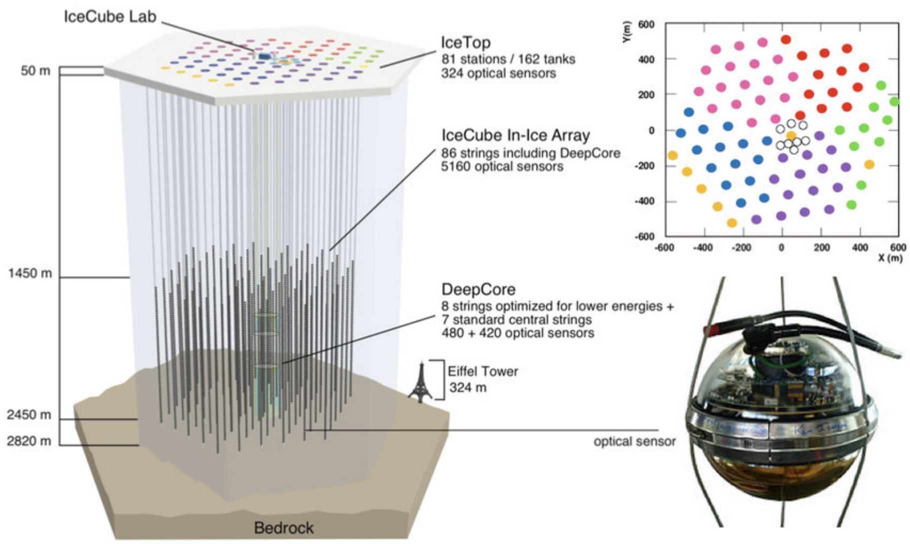

Figure 1.1: IceCube Neutrino Observatory geometry. IceTop measures the surface footprint of the shower, including the electromagnetic and low-energy muon components, while the in-ice IceCube detector measures high-energy muons that penetrate deep into the Antarctic ice. (Choma et al., 2018).

The IceCube Neutrino Observatory provides a distinctive experimental geometry, it combines a deep in-ice detector with a surface air-shower array at the South Pole. The in-ice IceCube detector is a cubic-kilometre Cherenkov detector instrumented with 5160 Digital Optical Modules (DOMs) on 86 strings deployed between approximately 1450 m and 2450 m below the surface of the Antarctic ice (Aartsen et al., 2017). It reconstructs the direction, energy, and identity of penetrating particles through the Cherenkov light emitted. Above it, IceTop is a square-kilometre surface array with 81 stations, each containing two ice-Cherenkov tanks equipped with two DOMs, and it measures cosmic-ray air showers with primary energies from about 100 TeV to 1 EeV (Abbasi et al., 2013).

This geometry makes IceCube/IceTop a three-dimensional muon detector and neutrino telescope. IceTop measures the electromagnetic component and GeV-scale muons near the surface, from which the primary energy and arrival direction can be reconstructed. The in-ice detector measures high-energy muons, typically above about 400 GeV at the surface, which survive to roughly 1.5 to 2.5 km of the deep detector as tracks or bundles and are characterised through their deposited energy loss $\mathrm{d}E/\mathrm{d}X$. Because of this special geometry, coincident events can be observed and provide simultaneous information about the electromagnetic shower size and the penetrating high-energy muon component.

Current IceCube cosmic-ray studies use data from IceTop and coincidence events to reconstruct the all-particle energy spectrum and the mass composition of CR. The lateral distribution of tank signals is fitted to obtain the shower-size parameter S_{125}, the signal at 125 m from the shower axis, which is used as an IceTop energy proxy. The S_{125} parameter, together with the zenith angle θ, the in-ice energy loss $\mathrm{d}E/\mathrm{d}X$, and high-energy stochastic energy-loss observables arising from radiative interactions are combined in a neural-network reconstruction of primary energy and mass-sensitive quantities (Aartsen et al., 2019).

Measurements of the muon component are central to these studies because the muon content of an air shower depends on both the primary energy and the primary mass. IceTop measures GeV muons in the outer region of the shower footprint, where the electromagnetic signal is reduced and single-muon signals become more visible (Kang, 2023). The in-ice detector records TeV muon bundles in the deep ice, and these bundles probe the high-energy core of the same shower. The comparison of both measurements can test the consistency of hadronic-interaction models used in air shower simulations. A major motivation for such measurements is the so-called "muon puzzle". Several air-shower experiments have observed more muons than predicted by simulations, indicating that hadrons[1] production in the forward and high-energy phase space is not yet fully constrained. Existing IceCube/IceTop comparisons show that different hadronic-interaction models do not give a fully consistent interpretation of all composition-sensitive observables, especially when GeV and TeV muon measurements are compared (Abbasi et al., 2022).

Atmospheric muons and neutrinos are connected through the atmospheric conditions that control meson[2] decays and interactions in the cascade. IceCube studies seasonal variations of atmospheric muon rates because a warmer and less dense atmosphere allows more meson decay than re-interaction, thereby increasing atmospheric muon and neutrino production (Abbasi et al., 2025). Atmospheric muons therefore provide a high-statistics probe of the meson-production physics underlying the conventional atmospheric neutrino flux.

Within this experimental context, a study of the correlation between high-energy atmospheric muons and neutrinos using simulation data is well motivated. Existing IceCube/IceTop analyses have shown that the muon component is essential for composition studies and for testing hadronic-interaction models, while atmospheric neutrino interpretation depends on the same cosmic-ray and cascade physics. This thesis therefore examines CORSIKA simulations of atmospheric muons, muon neutrinos, and electron neutrinos at the IceCube observation level, before detector simulation, to determine how the common hadronic cascade links these lepton[3] components.

The following literature review traces how this problem has been approached in air-shower theory, IceCube cosmic-ray measurements, atmospheric muon and neutrino studies and analyses.

[1] A hadron is a particle made of quarks and bound by the strong interaction; examples relevant to this thesis include protons, neutrons, pions, and kaons.

[2] A meson is an unstable hadron composed of a quark and an antiquark; examples relevant to this thesis include pions and kaons.

[3] A lepton is a fundamental particle that does not undergo strong interactions; examples relevant to this thesis include muons, muon-neutrinos, and electron-neutrinos.

1.2 Literature review

Since the first discovery of cosmic rays by Victor Hess in 1912, the physical framework of cosmic rays and extensive air showers has been developed thoroughly over the past century. The physical rules of the cascade are developed in the book *Cosmic Rays and Particle Physics* by Gaisser, published in 1990 and updated in 2016 (Gaisser, 1990, Gaisser et al., 2016). The competition between meson decay and interaction channels is central to their treatment of CR and EAS physics that provides the theoretical background for this thesis. At lower energies, mesons and muons decay more readily, so atmospheric neutrinos are more abundant. At higher energies, time dilation makes particles live longer in the laboratory frame, and re-interaction or survival to observation level becomes more likely. Thus, the muon and neutrino components are not separate products of the shower, but are closely related through the meson-decay chain.

In the study of CR, dedicated simulation tools of EAS evolution in the atmosphere have been developed. The most widely used among these is CORSIKA, a Monte Carlo simulation package originally developed for the KASCADE experiment in Karlsruhe, Germany and first released in 1998 by Heck et al. (Heck et al., 1998). CORSIKA simulates the full shower development from the first hadronic interaction of the primary cosmic ray down to the observation level, tracking all secondary particles until they interact, decay, or reach the observation level. The work emphasises the indispensability of hadronic-interaction models, since the forward phase space and the highest energies relevant to cosmic-ray air showers are not fully constrained by collider data. CORSIKA therefore provides a controlled numerical laboratory in which the consequences of different interaction models, decay channels, and primary masses and energies can be studied.

A complementary approach to full MC shower simulation is provided by Matrix Cascade Equations framework, MCEq, developed by Fedynitch et al. in 2015 (Fedynitch et al., 2015). Rather than tracking individual particles through stochastic evolution in a fully developed shower, MCEq solves a system of coupled cascade equations for inclusive particle fluxes. This makes MCEq especially useful for fast calculations of atmospheric muon and neutrino fluxes over many model assumptions. The particle cascade is represented by interaction and decay terms, with gain terms from hadronic production and particle decay and loss terms from interaction and decay losses.

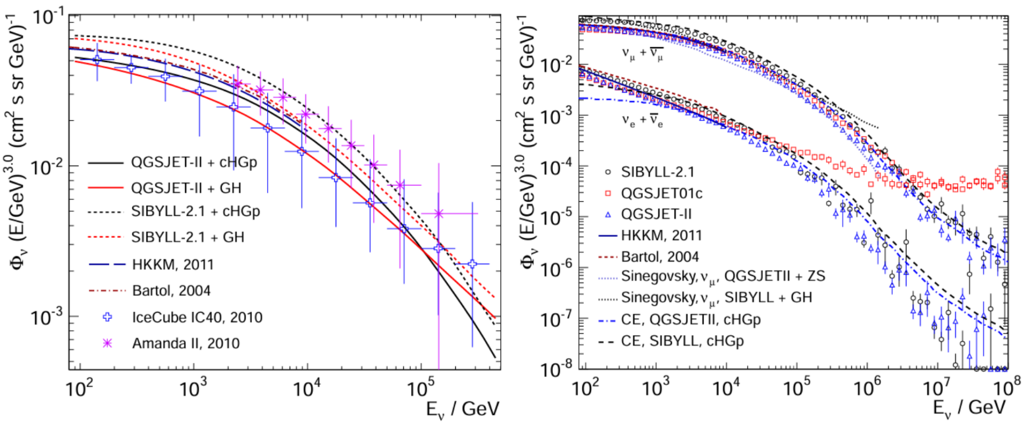

Figure 1.2: Conventional atmospheric neutrino fluxes calculated using cascade-equation methods and compared with experimental data. The figure illustrates how cascade-equation approaches can predict atmospheric muon-neutrino and electron-neutrino fluxes over a wide energy range, making them useful for benchmarking full Monte Carlo air-shower simulations such as CORSIKA. Result from Fedynitch et al. (2012)

The practical value of MCEq as a benchmark tool is demonstrated in the work *Influence of Hadronic Interaction Models and the Cosmic-Ray Spectrum on the High-Energy Atmospheric Muon and Neutrino Flux* by Fedynitch, Tjus and Desiati in 2012 (Fedynitch et al., 2012), which connects MC simulation with analytic cascade-equation predictions. The study uses CORSIKA to obtain inclusive yields of muons, muon neutrinos, and electron neutrinos at the surface and then uses these yields to calculate fluxes and lepton ratios. It shows that the predicted lepton fluxes depend strongly on the hadronic-interaction model, especially through the pion-to-kaon ratio, and also on the assumed primary cosmic-ray spectrum and composition.

The connection between CR and neutrinos extends beyond atmospheric physics in the review *High-energy Neutrino Astronomy: The Cosmic Ray Connection* by Halzen and Hooper in 2002 (Halzen and Hooper, 2002). Their review frames neutrinos as messengers from cosmic accelerators: if nature accelerates hadrons to extreme energies, then interactions near the source or during propagation should also produce high-energy neutrinos. This idea gives neutrino astronomy its larger motivation. However, it also introduces a difficulty: the atmospheric neutrino background. Before one can identify an astrophysical neutrino, one must understand the atmospheric neutrinos and atmospheric muons produced by ordinary cosmic-ray air showers. The atmosphere is therefore the first "laboratory" in which the cosmic-ray-neutrino connection must be understood.

The standard picture of air-shower development is well established, and the main features of the cosmic-ray spectrum have been observed by multiple experiments including KASCADE-Grande, IceCube/IceTop, Auger-HEAT, Tunka, TA-TALE, and LHAASO (Kang, 2022, 2025). IceCube enters this story as both a neutrino telescope and a detector of atmospheric muons. In the article *Characterization of the Atmospheric Muon Flux in IceCube* by Aartsen et al. published in 2016 (Aartsen et al., 2016), atmospheric muons are treated as a high-statistics signal that carries information about primary cosmic rays, hadronic interaction models, and possible prompt lepton contributions. Yet the same work also exposes a central limitation: the interpretation of atmospheric muons depends strongly on assumptions about cosmic-ray composition and hadronic particle production, which are themselves, not yet fully understood.

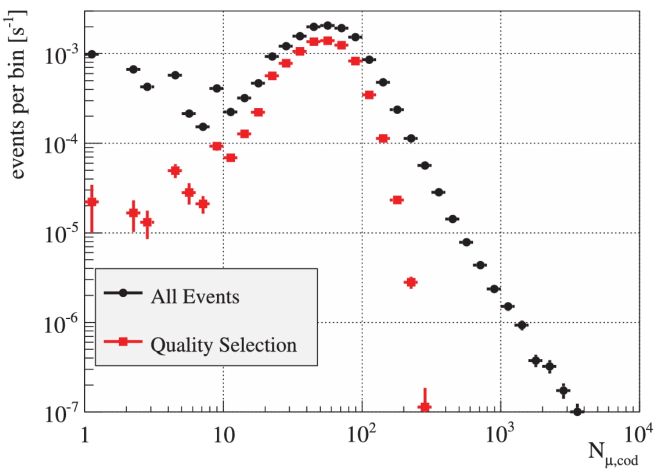

Figure 1.3: Distribution of reconstructed atmospheric muon-bundle multiplicity at the point of closest approach to the IceCube detector center for simulated events with 3000-4000 registered photoelectrons. The black points show the trigger-level sample, while the red points show the final high-multiplicity quality-selected sample. This observable demonstrates how IceCube can use atmospheric muon bundles as a probe of cosmic-ray air showers. Result from Aartsen et al. (2016).

In the current work *Recent Results of Cosmic-Ray Studies with IceTop at the IceCube Neutrino*

Observatory by Kang in 2023 (Kang, 2023), this limitation sharply comes into focus. The unique geometry, which allows the coincidence technique, makes IceCube sensitive to both the electromagnetic shower size and the high-energy muon bundle. Dr. Kang emphasises that the muonic component is crucial for mass-composition studies, but also that simulations based on current hadronic interaction models often underpredict the number of muons observed in air-shower experiments. This "muon puzzle" is one of the strongest reasons to study muons and neutrinos together rather than in isolation. The correlation between high-energy muons and neutrinos at the IceCube observation level can therefore provide insights into the hadronic interactions and meson decay processes that shape air showers.

The cosmic-ray setting of this problem is reviewed in the later paper of Dr. Kang and Dr. Haungs in 2024 *The Cosmic-Ray Spectrum in the PeV to EeV Energy Range* (Kang and Haungs, 2024). Their work places IceCube and IceTop within the wider question of the knee, the second-knee region, and the transition from galactic to extragalactic cosmic rays. Around the PeV scale, the all-particle spectrum steepens, and the mass composition is expected to change as lighter nuclei reach their acceleration or confinement limits earlier than heavier nuclei. This matters directly for the present thesis because proton and iron primaries do not generate identical showers. With a superposition model, an iron nucleus behaves approximately as 56 independent nucleons, producing a different shower-development profile and a different balance between muons, muon neutrinos and electron neutrinos at observation level. Therefore, the correlation between high-energy muons and neutrinos can be expected to differ between proton and iron primaries, and studying this difference can help us understand how primary mass affects shower development and the resulting particle fluxes at IceCube.

Taken together, while the production of atmospheric muons and neutrinos is well understood at the level of the basic decay chain and IceCube has measured both atmospheric muons and atmospheric neutrinos with high precision, the detailed correlation between high-energy muons and neutrinos at the IceCube observation level is still not fully examined. Since both particle populations originate mainly from the decay of charged pions and kaons, their energies and multiplicities are physically connected. However, this connection is modified by meson interaction and decay probabilities, atmospheric propagation, shower-to-shower fluctuations, and the mass and energy of the primary cosmic ray. Studying the joint behaviour of muons and neutrinos may therefore provide additional information about air-shower development and help clarify how the primary mass influences the secondary-particle fluxes observed by IceCube. This thesis investigates that using CORSIKA simulations of proton- and iron-induced showers with different primary energies. The MCEq framework is also used for the first time for comparison with CORSIKA. The simulated data will be analysed to characterise the correlation between the energy spectra of high-energy muons and neutrinos at the IceCube observation level.

1.3 Main questions and objectives

This thesis investigates the correlation between high-energy muons and neutrinos in extensive air showers at the IceCube observation level. The central research question is:

How are the energy spectra and production of high-energy muons and neutrinos correlated in extensive air showers at the IceCube observation level?

This question is addressed through the following specific research questions:

1. How do the energy spectra of muons and neutrinos depend on primary mass, primary

energy, and zenith angle?

2. Are the average lepton production yields simulated with CORSIKA consistent with the calculations predicted by MCEq under the same physical configuration?

3. What quantitative relationship exists between the number of muons and neutrinos produced in the same air shower?

4. Can the observed spectra and correlation patterns be interpreted in terms of the underlying shower physics?

The objectives of this thesis are to understand the cascade equations description and the physical background of EAS development, using CORSIKA as the main simulation framework and benchmarking its result with MCEq, and to analyse the production of atmospheric muons and neutrinos for different primary cosmic-ray conditions. In particular, the study extracts muon, muon-neutrino, and electron-neutrino spectra from CORSIKA simulations, after the benchmarking with MCEq, and investigates how differences between proton and iron showers arise from hadronic cascades to the observation level, under a primary energy and zenith range. The final objective is to represent and interpret the simulated muon-neutrino correlation in a form relevant for IceCube air-shower studies.

The scope of this thesis is limited to a simulation-based study, it does not attempt to reconstruct real IceCube data or perform a full detector-response analysis. Instead, it examines the physical content of CORSIKA shower outputs and compares their average behaviour with MCEq cascade equation calculations. This allows the study to focus on the underlying shower physics and the muon-neutrino correlation without the additional complexity of detector effects, which can be addressed in future work. The analysis is also limited to proton and iron primaries, which represent the extremes of the cosmic-ray mass spectrum. While this choice allows for a clear comparison of shower development between light and heavy primaries, it does not capture the full range of possible primary masses or the effects of mixed composition. Therefore, the results should be interpreted as illustrative of general trends rather than as definitive predictions for all cosmic-ray showers. The analysis is also restricted to conventional muons and neutrinos produced through standard pion, kaon, and muon decay channels in the hadronic cascade; prompt leptons arising from charm-hadron decays are not included.

Chapter 2

Theoretical Background

2.1 Cosmic Rays: Source Candidates and Acceleration Mechanisms

Cosmic rays are high-energy particles originating from outer space. These particles strike the Earth's atmosphere at a rate of about 1000 particles per meter squared per second at the top of the atmosphere, and the observed composition near Earth consists of roughly 90% protons, 9% helium nuclei, and 1% heavier nuclei, with a small fraction of electrons and gamma rays (Gaisser et al., 2016). Their energies extend from the relativistic GeV range to ultra-high energies of order 10^{20} eV (Gaisser et al., 2016), making them the most energetic particles known in nature.

The origin of cosmic rays is still not completely established. The majority of the cosmic-ray flux is understood to be of Galactic origin, while Solar cosmic rays form only a small and variable component associated with energetic solar events. At the highest energies, the gyroradii of charged particles in typical Galactic magnetic fields become comparable to, or larger than, the size of the Galaxy, suggesting an extragalactic origin for ultra-high-energy cosmic rays (Gaisser et al., 2016). The central source problem is therefore twofold: identifying the astrophysical accelerators capable of producing such high energies, and understanding the physical mechanisms responsible for that acceleration. Supernova remnants, active galactic nuclei, and gamma-ray bursts are among the leading candidates for cosmic-ray sources, but definitive associations remain elusive. Since charged particles are deflected by Galactic and intergalactic magnetic fields while propagating through the interstellar medium, the arrival direction of an observed cosmic ray does not directly point back to its source. Instead, source information must be inferred statistically from the energy spectrum, mass composition, arrival-direction anisotropy, and associated secondary particles such as neutrinos and gamma rays.

Supernova remnants are a leading candidate for the sources of Galactic cosmic rays. The power requirement for maintaining the observed cosmic-ray energy density in the galaxy is of order $L_{CR} \sim 7 \times 10^{40}$ erg s^{-1} (Gaisser et al., 2016, p. 237). This value is naturally comparable to the mechanical energy released by supernova explosions. After a supernova explosion, the ejected material expands supersonically into the surrounding interstellar medium and drives a shock wave into the circumstellar or interstellar medium. Charged particles near the shock scatter on magnetic irregularities in the plasma and may cross repeatedly between the upstream, unshocked gas and the downstream, shocked gas. The average fractional energy gain per shock-crossing is approximately:

$$\xi = \frac{\Delta E}{E} \approx \frac{4}{3}\left(\frac{u_1 - u_2}{c}\right), \tag{2.1}$$

where u_1 is the upstream flow speed and u_2 is the downstream flow speed, both measured in the shock frame (Gaisser et al., 2016, p. 241). The acceleration mechanism of supernova remnants is known as "diffusive shock acceleration", also called "first-order Fermi acceleration".

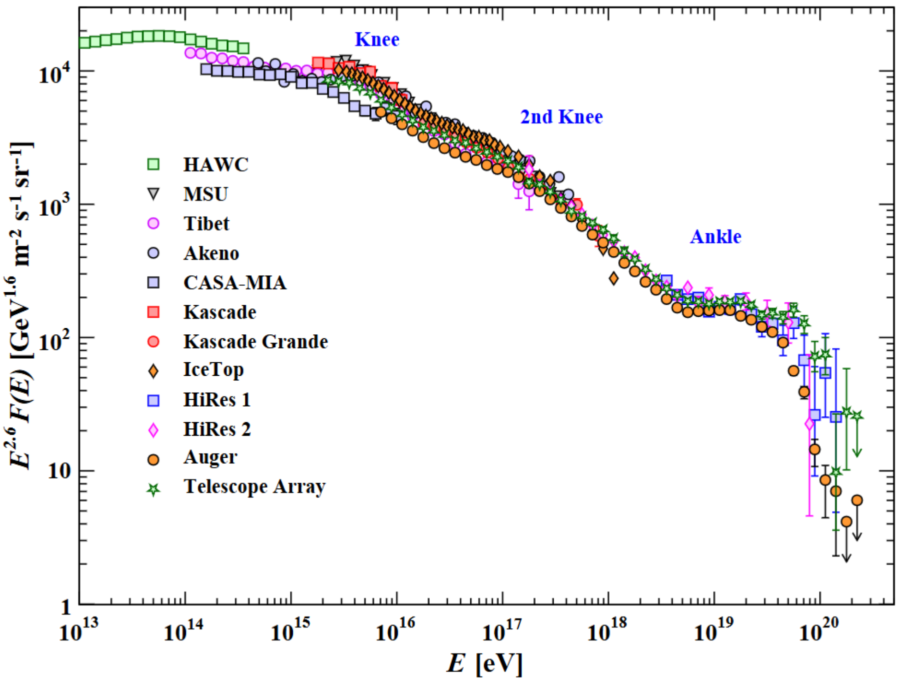

Figure 2.1: All-particle cosmic-ray energy spectrum measured by air-shower experiments. The flux is multiplied by $E^{2.6}$ to make spectral structures visible, including the knee, second knee, and ankle. These features mark changes in the cosmic-ray spectrum and motivate indirect air-shower studies in the PeV–EeV energy range. Result from the Particle Data Group cosmic-ray review Beatty et al. (2022); data references are listed in Alfaro et al. (2017), Fomin et al. (1991), Amenomori et al. (2008), Nagano et al. (1984), Glasmacher et al. (1999), Antoni et al. (2005), Apel et al. (2011), Andeen et al. (2019), Abbasi et al. (2008), Aab et al. (2020b,a), Abreu et al. (2021), Ivanov et al. (2019), Abbasi et al. (2018).

This acceleration process naturally produces a power-law spectrum and also provides a interpretation of the "knee" in the cosmic-ray spectrum. The all-particle spectrum steepens at around $3-5 \times 10^{15}$ eV (**Figure 2.1**). If this feature reflects the maximum rigidity to which Galactic accelerators can accelerate particles, then protons should cut off first at around a few PeV, followed by helium nuclei at around 10 PeV, CNO group at around 100 PeV and finally iron nuclei at around 300 PeV, because the maximum energy scales approximately with charge:

$$E_{max} \approx Ze\beta BR, \tag{2.2}$$

where Ze is the nuclear charge, $\beta = u/c$, B is the magnetic field strength, and R is the size of the acceleration region (Gaisser et al., 2016, p. 255). This rigidity-dependent cutoff scenario is called the Peters cycle and is consistent with measurements of the energy spectrum and mass composition in the knee region, which show a trend of increasing average mass with energy.

At higher energies above the ankle around 3 EeV, ultra-high-energy nuclei propagating over extragalactic distances lose energy through interactions with cosmic background radiation fields, such as the cosmic microwave background. This leads to the energy-loss processes including pion production around 7×10^{19} eV, and electron-positron pair production 6×10^{17} eV (Gaisser et al., 2016, p. 205). Therefore, the transition from galactic to extragalactic cosmic rays is expected to occur somewhere between 10^{17} eV and 10^{19} eV, but the exact energy and composition at this transition remain uncertain.

For this reason, high-energy gamma rays and neutrinos are important complementary messengers for cosmic-ray studies. Since they are neutral and weakly interacting, they can escape dense astrophysical environments. Neutrinos propagate over cosmological distances with negligible attenuation or deflection, while gamma rays travel in straight lines but may be absorbed through interactions with background radiation. Therefore, they can provide direct information about the sources and acceleration mechanisms of CR. However, they are also more difficult to detect, and their fluxes are generally much lower, especially at the highest energies. This motivates the study of atmospheric muons and neutrinos as a way to understand the connection between CR and neutrinos in the context of air showers, which is relevant for interpreting IceCube data and for testing hadronic-interaction models.

The source discussion in this thesis is restricted mainly to Galactic cosmic rays, for which supernova remnants remain the leading source candidates, since the simulated primary energies lie below and around the knee region rather than in the ultra-high-energy regime.

2.2 Air Showers and Hadronic Interaction Models

2.2.1 Air Shower Physics

The all-particle cosmic-ray spectrum approximately follows a power-law distribution, and its steeply falling flux makes direct measurements by satellite or balloon-borne experiments statistically limited above about 10^{14} eV to 10^{15} eV (Kang and Haungs, 2024); above this range, CR must be studied indirectly through EAS produced in the atmosphere. An extensive air shower begins when a high-energy primary cosmic ray enters the atmosphere and interacts with an atmospheric nucleus. The shower contains coupled hadronic, electromagnetic, and muonic components. The electromagnetic component is fed mainly by neutral pion decay, $\pi^0 \to \gamma + \gamma$, whereas the muonic component is produced mainly through the decay of charged hadrons, especially charged pions and kaons.

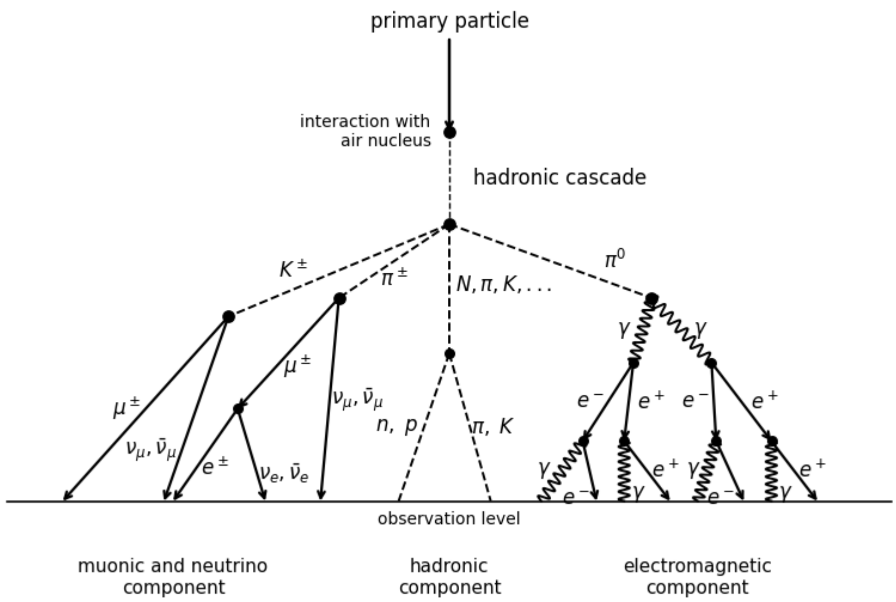

Figure 2.2: A simplified schematic of an EAS initiated by a high-energy cosmic-ray primary in the atmosphere. The first hadronic interaction produces secondary mesons and hadrons. Charged pions and kaons decay into muons and neutrinos, while neutral pions feed the electromagnetic cascade through photon production.

To understand the main features of hadronic air-shower development, several analytical models have been proposed. One of the most widely used is the Heitler-Matthews model (Matthews, 2005). In this model, a hadron of energy E produces n_{tot} secondaries with energy E/n_{tot}, with approximately two-thirds charged pions and one-third neutral pions (Gaisser et al., 2016, p. 315). The neutral pions immediately feed the electromagnetic cascade, while charged pions continue to interact if their energies exceed a typical decay energy E_{dec}. Once the charged hadrons fall below E_{dec}, they decay and produce muons. After several hadronic generations, most of the primary energy has been transferred to the electromagnetic component, while the remaining charged-meson component determines the muon yield. After about six hadronic generations, roughly 90% of the initial shower energy is eventually carried by electromagnetic particles and deposited as ionisation energy in the atmosphere (Gaisser et al., 2016, Meurer et al., 2006).

Another useful model that provides the standard first approximation for nuclear primaries is the superposition model. A nucleus of mass number A and total energy E_0 is treated approximately as A independent nucleons, each with energy E_0/A. This means that iron and proton showers of the same total energy do not develop identically. Heavier nuclei like iron interact earlier and develop higher in the atmosphere, while proton showers can penetrate more deeply. For the muon content, the superposition model predicts that the number of muons and depends on the primary mass. At the same total primary energy, iron showers contain about 40% more muons than proton showers and reach shower maximum approximately $80 - 100\ \mathrm{g\,cm^{-2}}$ higher in the atmosphere (Gaisser et al., 2016, p. 320). This statement is useful as theoretical context, but it must be applied carefully at IceCube observation level because muon survival, energy threshold, zenith angle, and observation altitude can affect the number of muons that actually reach the detector.

2.2.2 Hadronic Interaction Models

Because air-shower observables are indirect, simulations must use models to describe interactions of the cosmic rays and the atmospheric nuclei and the development of the cascade. In CORSIKA, the first few generations with high-energy hadronic interactions may be described by models such as SIBYLL, EPOS, QGSJet, etc., and use models like FLUKA or GHEISHA later in the cascade, where we have mostly low-energy hadronic interactions. The electromagnetic component can either be simulated with EGS4 or approximated using analytic NKG parameterisation. In this thesis, we use SIBYLL, FLUKA, and EGS4, a commonly used CORSIKA configuration for extensive air shower simulations in current cosmic-ray studies at IceCube observation level. The detail information on the main goals and physics underlying of these models is further discussed in the **Appendix A**, section **Hadronic Interaction Models**.

2.3 Muons and Neutrinos Production in Air Showers Development

After the hadronic cascade has produced charged pions and kaons, the atmospheric muon and neutrino yields are governed mainly by the competition between meson decay and meson reinteraction in the atmosphere. The conventional atmospheric lepton component is produced predominantly through the weak two-body decays $\pi^\pm \to \mu^\pm + \nu_\mu(\bar{\nu}_\mu)$ and $K^\pm \to \mu^\pm + \nu_\mu(\bar{\nu}_\mu)$, where the charged-pion channel has an almost 100% branching ratio, while the charged-kaon channel has a branching ratio of about 63.5% (Gaisser et al., 2016, p. 127). The muons produced in these decays may subsequently decay through $\mu^\pm \to e^\pm + \nu_e(\bar{\nu}_e) + \nu_\mu(\bar{\nu}_\mu)$. Thus, when the full pion decay chain proceeds without atmospheric suppression, one charged pion produces one muon, two muon-neutrinos, and one electron-neutrino. This gives the approximate production-level flavour ratio

$$\frac{\nu_\mu + \bar{\nu}_\mu}{\nu_e + \bar{\nu}_e} \simeq 2. \tag{2.3}$$

This relation is valid mainly at low energies, when considering all muons decays. At high energies, muons often reach the observation level before decaying, reducing the electron-neutrino contribution from muon decay (Gaisser et al., 2016). Consequently, the electron-neutrino flux becomes increasingly suppressed relative to the muon-neutrino flux at higher energies.

The connection between muons and neutrinos is also fixed by the decay kinematics of their parent mesons. For a relativistic two-body decay $M \to \mu + \nu_\mu$, where $M = \pi^\pm$ or $K^\pm$, define

$$r_M = \frac{m_\mu^2}{m_M^2}. \tag{2.4}$$

The daughter-particle energies in the laboratory frame are then bounded by

$$r_M E_M \le E_\mu \le E_M, \quad 0 \le E_\nu \le (1 - r_M) E_M,$$

where E_M is the energy of the parent meson (Gaisser et al., 2016, p. 128-129). For pion decay, the average energy fractions are approximately $\langle E_\mu \rangle \simeq 0.79 E_\pi$, $\langle E_{\nu_\mu} \rangle \simeq 0.21 E_\pi$, and $\langle E_\mu \rangle \simeq 0.52 E_K$, $\langle E_{\nu_\mu} \rangle \simeq 0.48 E_K$ (Gaisser et al., 2016, p. 129). The decay probability per unit slant depth of a secondary meson is controlled by its critical energy. For a particle i, the critical energy is defined as

$$\epsilon_i = \frac{m_i c^2 h_0}{c\tau_i}, \tag{2.5}$$

where m_i is the particle mass, τ_i is its lifetime, and h_0 is the atmospheric scale height (Gaisser et al., 2016, p. 122). The critical energy ϵ_i is the characteristic energy at which decay and interaction become comparable in the atmosphere. The characteristic values of pion and kaon are approximately $\epsilon_\pi \simeq 115$ GeV and $\epsilon_K \simeq 850$ GeV (Gaisser et al., 2016, Table 5.3). Thus the charged pions begin to be suppressed by re-interaction at lower energy than charged kaons, which is why kaons become increasingly important for high-energy atmospheric neutrino production. This definition follows from Gaisser's treatment of exponential atmosphere and the conversion of decay length into atmospheric depth (Gaisser et al., 2016).

The development of the cascade of particles in the atmosphere can be described by the coupled cascade equations. For a secondary particle i, the cascade equation describes how its flux changes with atmospheric slant depth X. It contains loss terms from both interaction and decay of the particle i, and gain terms from interaction or decay of its higher-energy parent particles. For charged pions, neglecting pion-kaon coupling and writing only the pion-nucleon sector, the transport equation is schematically expressed as

$$\begin{aligned} \frac{d\Pi(E,X)}{dX} = & -\left(\frac{1}{\lambda_\pi} + \frac{\epsilon_\pi}{EX\cos\theta}\right)\Pi(E,X) \\ & + \frac{1}{\lambda_\pi}\int_0^1 \Pi\left(\frac{E}{x_L}, X\right) F_{\pi\pi}(x_L)\frac{dx_L}{x_L^2} \\ & + \frac{Z_{N\pi}}{\lambda_N} N(E,0) e^{-X/\Lambda_N}. \end{aligned} \tag{2.6}$$

Here $\Pi(E, X)$ is the charged-pion flux, $N(E, 0)$ is the primary nucleon flux at the top of the atmosphere, λ_π and λ_N are interaction lengths in air, $EX \cos\theta/\epsilon_\pi \equiv d_\pi$ is the pion decay length expressed in $\mathrm{g\,cm^{-2}}$, and $F_{\pi\pi}(x_L)$ is the inclusive production function for producing pions (Gaisser et al., 2016, p. 124). The first term removes pions by hadronic interaction and decay, the second term regenerates pions through pion-air interactions, and the last term injects pions from nucleon-air interactions.

The approximate analytic solution for this equation can be obtained by assuming that, under the regeneration integral, the pion flux can be factorised into a into a power-law energy dependence and a slant depth dependent function. This is justified since the source term is driven by the primary nucleon spectrum, which is itself approximated as a power law. With this ansatz, the pion interaction and regeneration terms are combined into a single effective attenuation length Λ_π, giving

$$\frac{\mathrm{d}\Pi}{\mathrm{d}X} = -\Pi(E, X)\left(\frac{1}{\Lambda_\pi} + \frac{\epsilon_\pi}{EX\cos\theta}\right) + \frac{Z_{N\pi}}{\lambda_N} N_0(E) e^{-X/\Lambda_N}, \tag{2.7}$$

where $Z_{N\pi}$ is the spectrum-weighted moment for pion production by nucleons, and Λ_N is the nucleon attenuation length (Gaisser et al., 2016, p. 124). From this equation, we can get the corresponding integral solution, which interpolates between the high-energy and low-energy limits. The exact solution (Gaisser et al., 2016, p. 124) of this equation is

$$\Pi(E, X) = e^{-(X/\Lambda_\pi)} \frac{Z_{N\pi}}{\lambda_N} N_0(E) \int_0^X e^{\left(\frac{X'}{\Lambda_\pi} - \frac{X'}{\Lambda_N}\right)} \left(\frac{X'}{X}\right)^{\epsilon_\pi/E\cos\theta}. \tag{2.8}$$

In the high-energy limit, when $E\cos\theta \gg \epsilon_i$, $(X'/X)^{\epsilon_\pi/E\cos\theta} \longrightarrow 1$, the exponent tends to zero, so the decay term becomes negligible, and the solution is interaction dominated. Physically, this means that a relativistic pion or kaon has a long time-dilated lifetime, so it is more likely to collide with an air nucleus before it decays. For charged pions, the high-energy solution (Gaisser et al., 2016, p. 122) is given as

$$\Pi(E, X) = N(E, 0) \frac{Z_{N\pi}}{1 - Z_{NN}} \frac{\Lambda_\pi}{\Lambda_\pi - \Lambda_N} \left(e^{-X/\Lambda_\pi} - e^{-X/\Lambda_N}\right). \tag{2.9}$$

The production of muons and neutrinos from its decay channels is suppressed by an additional factor proportional to $\epsilon_i/(E\cos\theta)$. Therefore, the atmospheric lepton spectrum becomes steeper than the primary spectrum at high energy.

In the low-energy limit $E\cos\theta \ll \epsilon_\pi$, $(X'/X)^{\epsilon_\pi/E\cos\theta}$ is small except when X' near X, decay dominates over re-interaction. The solution (Gaisser et al., 2016, p. 125) becomes

$$\Pi(E, X) \simeq \frac{Z_{N\pi}}{\lambda_N} N(E, 0) e^{-X/\Lambda_N} X \frac{E\cos\theta}{\epsilon_\pi}. \tag{2.10}$$

Because low-energy pions decay quickly after being produced, the corresponding muon and neutrino production is large.

The same treatment can be applied to kaons and other hadrons.

The dependence on $E\cos\theta$ also explains the zenith-angle dependence of the atmospheric muon and neutrino production. For the parent mesons $\pi^\pm$ and $K^\pm$, a more inclined shower, increasing zenith angle θ decreases $E\cos\theta$ making a shorter decay length $d_{\pi^\pm}$ or $d_{K^\pm}$. This means that the decay probability is larger for inclined showers, therefore, pions and kaons in inclined showers are more likely to decay than the same-energy pions and kaons in vertical showers.

For the muons themselves, the situation is different. The muon decay rate per atmospheric depth (Gaisser et al., 2016, p. 133) is

$$\frac{\mathrm{d}N_\mu}{\mathrm{d}X} = -\frac{\epsilon_\mu}{EX\cos\theta} N_\mu(E, X), \tag{2.11}$$

The muon decay probability is inversely proportional to $E\cos\theta$, this means that a longer inclined path gives low-energy muons more time and material to decay or lose energy due to ionisation before reaching the observation level. High-energy muons, on the other hand, have a long time-dilated lifetime and can survive to the surface, while only the most energetic muons can penetrate deep enough to reach the in-ice IceCube detector.

The high-energy approximation for the atmospheric muon flux (Gaisser et al., 2016, p. 134) is

$$\frac{\mathrm{d}N_\mu}{\mathrm{d}E_\mu} \simeq \frac{0.14E_\mu^{-2.7}}{cm^2\ s\ sr\ GeV}\left[\frac{1}{1+1.11E_\mu\cos\theta/115\ GeV} + \frac{0.054}{1+1.11E_\mu\cos\theta/850\ GeV}\right]. \tag{2.12}$$

The first term is associated with pion decay, and the second term is associated with kaon decay. This expression is valid mainly at sufficiently high energies, where muon decay and ionisation losses in the atmosphere are less important.

The relation between an observed muon and the energy of the primary cosmic ray can be understood through a differential response curve,

$$R_\mu = \frac{\mathrm{d}N_\mu(>E_\mu)}{\mathrm{d}\ln E_0}, \tag{2.13}$$

which gives the distribution of primary energies E_0 that contributing to a measured muon signal (Gaisser et al., 2016, p. 135). For vertical muons with $E_\mu > 20$ GeV at sea level, the median primary energy is about 280 GeV per nucleon, while the mean primary energy is about 750 GeV per nucleon because the response distribution has a long high-energy tail (Gaisser et al., 2016).

A compact approximation for the conventional atmospheric neutrino flux is

$$\frac{\mathrm{d}N_\nu}{\mathrm{d}E_\nu} \simeq \frac{N_0(E_\nu)}{1-Z_{NN}}\left[\frac{A_{\pi\nu}}{1+B_{\pi\nu}E_\nu\cos\theta/\epsilon_\pi} + 0.635\frac{A_{K\nu}}{1+B_{K\nu}E_\nu\cos\theta/\epsilon_K}\right], \tag{2.14}$$

where $N_0(E_\nu)$ is the primary nucleon flux, Z_{NN} is the nucleon regeneration moment, and the coefficients A and B describe meson production, decay kinematics, and atmospheric attenuation (Gaisser et al., 2016, p. 132). The first term describes the charged-pion contribution, while the second term describes the charged-kaon contribution. The equation shows explicitly that the atmospheric neutrino flux is controlled by the primary spectrum, meson production, zenith angle, and the different critical energies of pions and kaons.

At production, atmospheric neutrino fluxes show a clear energy-dependent flavour ratio. Below about 2 GeV, the ratio of muon-neutrino to electron-neutrino is close to 2 because the full pion-muon decay chain usually completes (Gaisser et al., 2016). As energy increases, the muon-decay contribution decreases, which steepens the neutrino spectrum and affects ν_e more strongly than ν_μ. For energies below about a TeV, neutrino absorption in the Earth is negligible, so upward and downward fluxes would be symmetric in the absence of flavour oscillations (Gaisser et al., 2016). The observed path-length dependence of the muon-neutrino to electron-neutrino ratio was therefore essential to the discovery of atmospheric neutrino oscillations. However, in this thesis, the CORSIKA simulation does not account for neutrino oscillations, so the fluxes are symmetric and the production mechanism determines the flavour ratio.

For this thesis, the correlation between N_μ, N_{ν_μ}, and N_{ν_e} is expected to depend on secondary-particle energy, zenith angle, primary mass, and observation level. A strong N_μ-N_{ν_μ} correlation is expected when both observables are dominated by the same charged-pion and charged-kaon parents. The N_μ-N_{ν_e} correlation is expected to be weaker and more energy dependent, because high-energy electron-neutrinos are less directly tied to pion decay and become more dependent on kaon decay and on whether the intermediate muon decays before reaching the ground. The next chapter describes the CORSIKA simulation setup and the analysis workflow used to study these correlations.

Chapter 3

Materials and Methods

3.1 Materials: CORSIKA simulation

CORSIKA (Heck et al., 1998) is a Monte Carlo program for simulating extensive air showers and tracking secondary particles through the atmosphere until they interact, decay, or reach a selected observation level. It records the particle type, energy, momentum, position, direction, and arrival time of secondary particles at observation level, which makes it suitable for studying the relation between muons and neutrinos before detector-response effects are introduced. In this thesis, CORSIKA was used as the main framework for full EAS simulations.

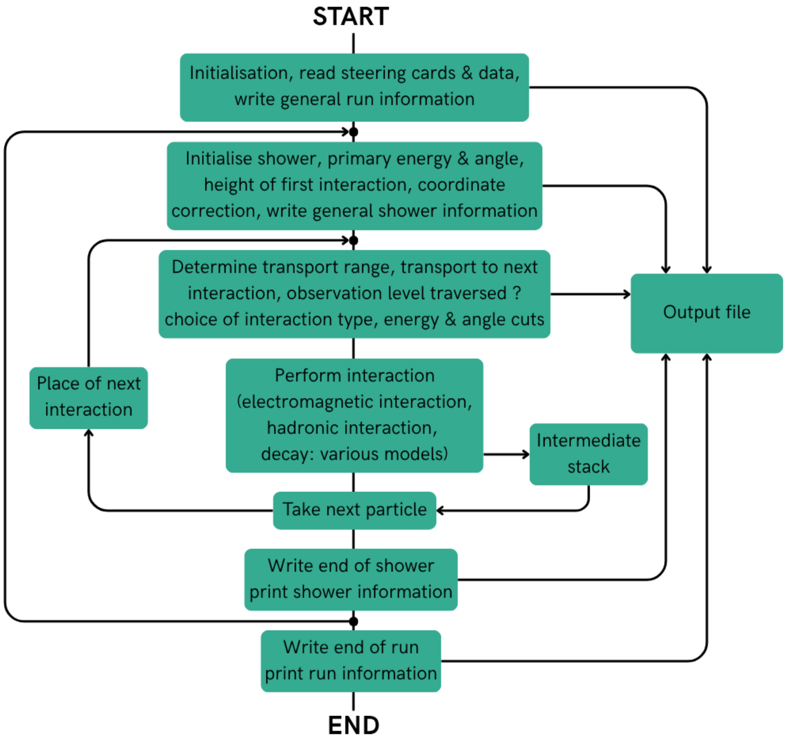

Figure 3.1: Simplified flow diagram of CORSIKA simulation workflow. The run begins with the initialisation of input steering cards. For each shower, CORSIKA defines the primary-particle energy, direction, first-interaction height, and coordinate corrections. Particles are then transported through the atmosphere until the next interaction point, decay, energy cut, angular cut, or observation-level crossing is reached. Electromagnetic interactions, hadronic interactions, and decays generate secondary particles, which are stored in the intermediate stack and propagated iteratively until the shower terminates. Particles crossing the observation level and summary information at shower and run level are written to the output file. Adapted from the CORSIKA 7.8050 User's Guide (Heck et al., 2025).

The workflow of an EAS simulation using CORSIKA is described in the **Figure 3.1**. Generations of secondary particles of a shower are stored in the intermediate particle stack, where each particle is stored and propagated until the full cascade has terminated (Heck et al., 1998). The shower evolution is treated as a sequence of particle transport, interaction, and decay processes, as determined by the hadronic interaction models. In CORSIKA, hadronic interactions are separated into high- and low-energy regimes, while the electromagnetic part of the shower is treated either by EGS4 (Nelson et al., 1985) or by the analytical NKG option (Lagutin et al., 1979). Before running a simulation, these models must be specified in the CORSIKA configuration.

3.1.1 CORSIKA Configuration

The CORSIKA executable used in this thesis was based on the **CORSIKA 7.8050** version and compiled in 64-bit mode. The high-energy hadronic interaction model was **SIBYLL 2.3d** (Riehn et al., 2020) for the main analysis and **SIBYLL 2.3e**[1] for the benchmark, the low-energy hadronic interaction model was **FLUKA**, and the electromagnetic component was simulated with **EGS4 + LPM option**. In CORSIKA 7.8050 (Heck et al., 2025), the SIBYLL option selects SIBYLL routines and their corresponding high-energy hadronic cross sections for hadron-nucleus and nucleus-nucleus interactions. The FLUKA option selects FLUKA routines for low-energy hadron-nucleus interactions, with the appropriate FLUKA cross sections. The EGS4 option explicitly follows electrons, positrons, and photons and their electromagnetic interactions in the atmosphere.

The executable was compiled with the additional options **LPM**, **NEUTRINO**, **CHARM**, **SLANT**, **CURVED**, and **UPWARD**. The LPM option selects the EGS4 routines that include the LPM effect. The NEUTRINO option explicitly tracks neutrinos emerging from pion, kaon, and muon decays, without treating neutrino interactions and oscillations. The SLANT option uses slant depth rather than vertical depth for longitudinal shower distributions. The CURVED option enables the treatment of very inclined geometries, where the curvature of the atmosphere becomes relevant. Although the executable included the CHARM option, the analysis in this thesis is restricted to conventional muons and neutrinos, prompt leptons from charm hadrons are not included in the interpretation (Heck et al., 2025).

3.1.2 CORSIKA Simulation Setup

Each CORSIKA run was controlled by an input file of the form `SIMnnnnnn.inp`. The input file contains steering cards that define the physical conditions under which each air shower is generated and therefore define the simulation phase space used later in the analysis. The main steering cards and their function are determined in the **Table A.2**.

In our simulations, we mainly generated one shower per run, `NSHOW` = 1. This means that each output file contains data of one shower, so each simulated file is only 30 MB up to 5 GB. The primary particles are proton and iron, `PRMPAR` = 14 or `PRMPAR` = 5626. The zenith angle `THETAP` are random in range from 0 – 65°, but for benchmarking, they are fixed at 15° and 60°.

3.1.3 CORSIKA Output Data

The output from a CORSIKA run is a binary file that contains particle-level information in the shower or, if enabled, a longitudinal profile file that contains the particle distribution as a function of atmospheric depth. In this thesis, we only analyse the binary output files.

The CORSIKA binary output files were converted into ROOT files for analysis, using the converter from CORSIKA libraries. Each ROOT file contains one event-level tree, `TTree:Event`, and a set of particle-level ntuples, `TNtupleD:data_1;n`, where n labels the shower index. The event-level tree stores one entry per shower, while the particle-level ntuples store the secondary particles that reach the observation level. This information is determined in the **Table 3.1** and **Table 3.2**

[1] Sibyll 2.3e is the latest version, it is the same as Sibyll 2.3d but with some asymmetry bug corrected.

Table 3.1: Event-level information stored in `TTree:Event`.

Variable	Meaning
`Eprim`	Primary energy in GeV.
`Theta`	Primary zenith angle in radians.
`Phi`	Primary azimuth angle in radians.
`Xmax`	Atmospheric depth of shower maximum in $\mathrm{g\,cm^{-2}}$.
`Nmax`	Maximum number of particles in the shower.
`Zfirst`	Height of the first interaction.
`Nph`	Number of photons.
`Nel`	Number of electrons and positrons.
`Nmu`	Number of muons.
`Nha`	Number of hadrons.
`Ntot`	Total number of particles.

Table 3.2: Particle-level information stored in `TNtupleD:data_1;n`.

Variable	Meaning
`id`	CORSIKA particle-identification code.
`ek`	Kinetic energy of the secondary particle in GeV.
`px`, `py`, `pz`	Momentum components in GeV/c.
`x`, `y`, `z`	Particle position at the observation level. In the converted output, particles are recorded at $z = 0$.
`t`	Particle arrival time in ns. The reference time depends on the CORSIKA timing option.
`w`	Particle weight, associated with thinning in Monte Carlo simulations.

The particle species were selected using the CORSIKA particle-identification code (Heck et al., 2025). Muons were selected as μ^+ : `id` = 5, μ^- : `id` = 6, electron neutrinos and antineutrinos as ν_e : `id` = 66, $\bar{\nu}_e$: `id` = 67, and muon neutrinos and antineutrinos as ν_μ : `id` = 68, $\bar{\nu}_\mu$: `id` = 69. Therefore, the total shower-level multiplicities used in the analysis were defined as

$$\begin{aligned} N_\mu &= N_{\mu^+} + N_{\mu^-}, \\ N_{\nu_\mu} &= N_{\nu_\mu} + N_{\bar{\nu}_\mu}, \\ N_{\nu_e} &= N_{\nu_e} + N_{\bar{\nu}_e}. \end{aligned}$$

The `w` parameter is associated with the particle weight when the thinning method is applied. In MC simulations, the output data can be very large if every particle in the shower is recorded. The thinning method helps reduce the output data size by replacing many secondary particles with a smaller number of representative particles carrying statistical weights. When particle weights were present in the ROOT output, the multiplicity in a selected sample S was computed as

$$N_s = \sum_{i \in S} w_i, \tag{3.1}$$

where w_i is the CORSIKA particle weight. For unthinned simulations, $w_i = 1$. In this thesis, we used unthinned simulations.

3.1.4 MCEq Framework and Benchmarking

In this work, MCEq (Fedynitch et al., 2015) numerical solver was used as a framework to benchmark the average lepton spectra obtained from CORSIKA. It solves the coupled cascade equation numerically in matrix form, rather than following each secondary particle shower by shower as in a MC simulation. This makes it suitable for testing whether the average CORSIKA muon and neutrino spectra are consistent with the independent deterministic calculation based on the same physical inputs.

In matrix form, the cascade equation is written as

$$\frac{d\mathbf{\Phi}}{dX} = \left[(-\mathbf{I} + \mathbf{C})\mathbf{\Lambda}_{\mathrm{int}} + \frac{1}{\rho(X)}(-\mathbf{I} + \mathbf{D})\mathbf{\Lambda}_{\mathrm{dec}}\right]\mathbf{\Phi}, \tag{3.2}$$

where $\mathbf{\Phi}$ is the vector of particle spectra, $\mathbf{C}$ is the interaction matrix, $\mathbf{D}$ is the decay matrix, and $\mathbf{\Lambda}_{\mathrm{int}}$ and $\mathbf{\Lambda}_{\mathrm{dec}}$ contain the reciprocal interaction and decay lengths (Fedynitch et al., 2015).

MCEq returns one deterministic solution for each input configuration of this matrix cascade equation. Therefore, its output is numerical solutions of particle fluxes of the cascade equations for a fixed set of inputs (primary flux, hadronic interaction model, atmosphere, and zenith angle), rather than a distribution over a whole shower as a MC simulation would produce.

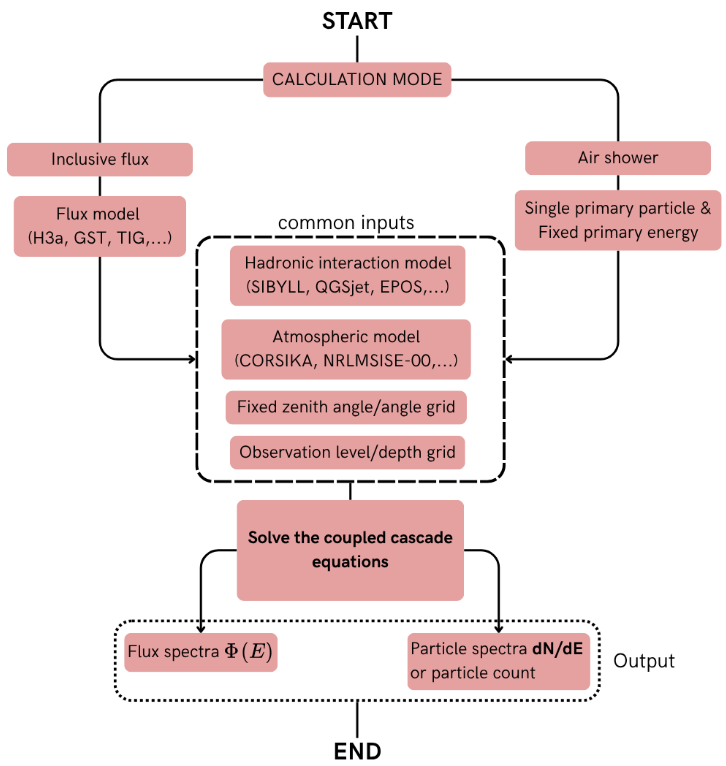

Figure 3.2: Simplified flow diagram of the two MCEq calculation modes and their main input and output quantities. In inclusive flux mode, the initial condition is a primary cosmic-ray flux model, and the output is a flux spectrum $\mathbf{\Phi}(E)$. In air-shower mode, the initial condition is a simple primary particle with fixed primary energy, and the output is a secondary-particle yield spectrum dN/dE or an integrated particle count over a selected energy interval. Both modes require common inputs such as the hadronic interaction model, atmospheric model, fixed zenith angle or grid of fixed angles, and observation level or depth grid before solving the coupled cascade equations.

The MCEq benchmark was performed before the main analysis. Its purpose was to check the consistency of the average CORSIKA lepton production against an independent cascade-equation solution. The comparison was made using the air-shower mode, its working flow is introduced in the **Figure 3.2**. The input configuration for the benchmark were proton and iron primaries at energy 10^{14} eV, zenith angles of 15° for vertical showers and 60° for inclined showers. Other required common inputs in the diagram are the CORSIKA South Pole-April atmosphere profile, the SIBYLL 2.3e hadronic interaction model, and the IceCube observation level at 2840 m.

The agreement between CORSIKA and MCEq was evaluated by comparing the secondary-particle spectra in the kinetic-energy bins. For each particle species h, the comparison quantity was the bin-wise ratio

$$R_i = \frac{(\mathrm{d}N_h/\mathrm{d}E)_{\mathrm{CORSIKA},i}}{(\mathrm{d}N_h/\mathrm{d}E)_{\mathrm{MCEq},i}}, \tag{3.3}$$

where i denotes the secondary-energy bin. The value $R_i = 1$ indicates complete agreement between the CORSIKA mean and MCEq deterministic solution. Values above unity indicate that CORSIKA predicts a larger yield than MCEq in that energy bin, while values below unity indicate a smaller yield. In this work, the ratio was used separately for $\mu^+ + \mu^-$, $\nu_\mu + \bar{\nu}_\mu$ and $\nu_e + \bar{\nu}_e$. Since the results from CORSIKA are the average of the particle yield from many showers, there is fluctuation from shower to shower and we need to determine its statistical uncertainty. Define $Y_{h,i}^{(k)}$ as the yield of particle species h in energy bin i for shower k in CORSIKA, the mean yield is

$$\bar{Y}_{h,i} = \frac{1}{N_{\mathrm{shower}}} \sum_{k=1}^{N_{\mathrm{shower}}} Y_{h,i}^{(k)}. \tag{3.4}$$

The uncertainty on the mean yield was estimated using the standard error of the mean (SEM),

$$\mathrm{SEM}_{h,i} = \frac{\sigma_{h,i}}{\sqrt{N_{\mathrm{shower}}}}, \tag{3.5}$$

where the standard deviation $\sigma_{h,i}$ is

$$\sigma_{h,i} = \sqrt{\frac{1}{N_{\mathrm{shower}} - 1} \sum_{k=1}^{N_{\mathrm{shower}}} (Y_{h,i}^{k} - \bar{Y}_{h,i})^2}. \tag{3.6}$$

This uncertainty reflects the shower-to-shower fluctuations in the finite CORSIKA sample. At high secondary energies, the number of particles per bin is often small, so the statistical uncertainty becomes large and these bins were excluded from quantitative comparisons.

3.2 Methods: Dataset and Workflow

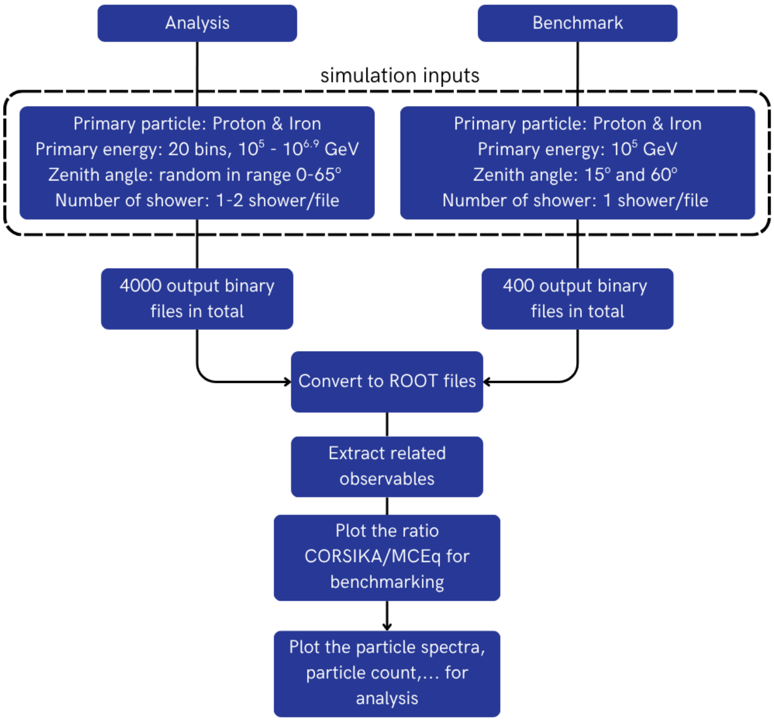

Figure 3.3: Analysis workflow for the CORSIKA simulation used in this thesis. The main analysis branch uses proton- and iron-induced showers over 20 primary-energy bins from 10^5 – $10^{6.9}$ GeV, with zenith angles randomly sampled between 0 – $65°$. The benchmark branch uses proton- and iron-induced showers at fixed primary energy 10^5 GeV and fixed zenith angles of $15°$ and $60°$. In both branches, the CORSIKA binary outputs are converted into ROOT files, from which the relevant observables are extracted and averaged for further analysis.

The main CORSIKA dataset used for the correlation analysis consists of proton- and iron-induced air showers in 20 primary-energy bins, covering $\log_{10}(E_{\mathrm{prim}}/\mathrm{GeV}) = 5.0, 5.1, ..., 6.9$, corresponding to $10^5 - 10^{6.9}$ GeV. For each primary type and energy bin, 100-200 showers were simulated. A preliminary statistical check was performed using 10 and 100 showers per energy bin. For 10 showers, the relative uncertainty on the mean particle yield,

$$\frac{\mathrm{SEM}}{\bar{N}} = \frac{\sigma/\sqrt{N_{\mathrm{shower}}}}{\bar{N}},$$

can still reach about 11% for some proton-muon samples. With 100 showers, it decreases to the percent level, below 3% for the total muon and neutrino yields. This gives a dataset of 100-200 showers statistical stability to study shower-to-shower fluctuations while keeping the analysis manageable within the available computing time and thesis scope.

The analysis workflow contains two main stages. The first stage was the preparation of the CORSIKA output, with the physics configurations of the simulations is provided in the **Figure 3.3**. The CORSIKA binary files were then converted into ROOT files. The event tree was used to obtain quantities such as the primary energy, zenith angle, and shower maximum, while the particle ntuples were used to extract the secondary particles reaching the observation level. The second stage was selected the related observables and made plots for analysis. The particle groups $\mu^+ + \mu^-$, $\nu_\mu + \bar{\nu}_\mu$, and $\nu_e + \bar{\nu}_e$, were selected and binned by kinetic energy. These binned multiplicities were then used for the CORSIKA-MCEq benchmark and further analysis.

Chapter 4

Results and Discussion

4.1 CORSIKA - MCEq Benchmarks

The CORSIKA-MCEq benchmark shows an overall good agreement between the Monte Carlo air-shower simulation and the deterministic cascade-equation calculation. The particle spectra from both primaries follow closely to the deterministic cascade-equation prediction lines over several orders of magnitude in secondary kinetic energy.

When comparing the vertical-shower benchmarks and the inclined-shower benchmarks, we can see that the inclined showers have a slightly closer agreement and less fluctuating than the vertical showers. We can explain this by considering the physical treatment of meson interactions and decay in both CORSIKA and MCEq. For more inclined showers, the mesons are more likely to decay. The meson decay is governed by well-known lifetimes, branching ratios, and two-body decay kinematics, it is relatively stable and is treated similarly in both frameworks. This can be the reason that makes the inclined-shower benchmark closer between the two approaches. For more vertical showers, the charged pions and kaons are more likely to re-interact before they decay. Re-interaction depends on hadronic interaction models. In CORSIKA, these processes are handled event by event, while in MCEq, it is numerically solved from the matrix cascade equation. Therefore, small deviations between these two approaches can become more visible in the vertical case.

An important difference appears in the low-secondary-energy bins of both primaries spectra. The CORSIKA/MCEq ratio R_μ is lower than unity by roughly 20% in the vertical-shower case and 10% in the inclined-shower case. In contrast, we observed that the CORSIKA/MCEq ratio R_{ν_e} is above unity by roughly the same order. Since electron-neutrino is mainly produced from muon decays, we can understand this difference as the low-energy muon yield from CORSIKA decays being greater than the low-energy muon yield from MCEq. This reflects a slightly different balance between muon survival and muon decay before reaching the observation level between CORSIKA and MCEq. Since this is the first time MCEq has been used to benchmark with CORSIKA, the observed differences are under discussion with IceCube collaborators.

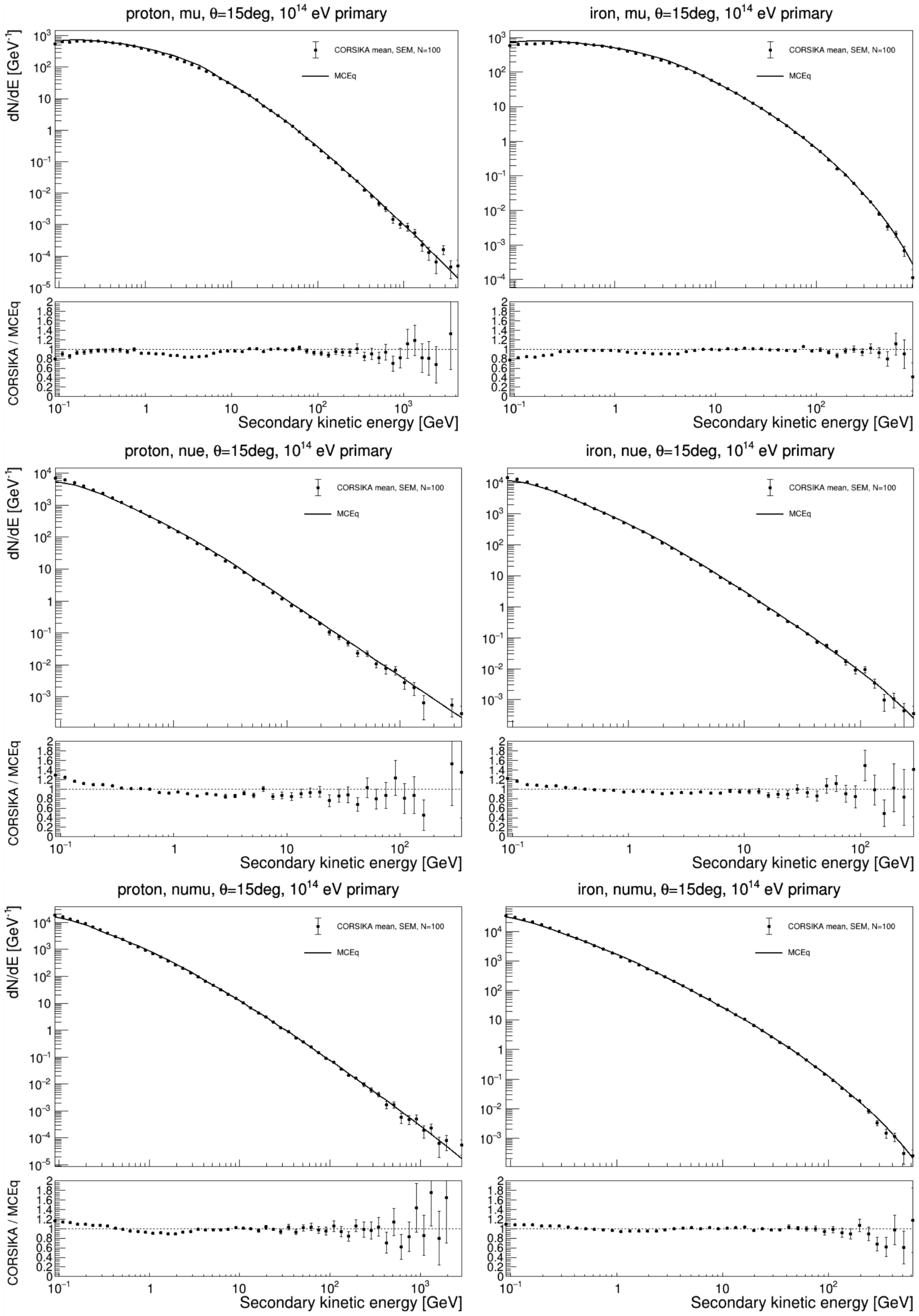

Figure 4.1: CORSIKA-MCEq benchmark of differential muon, muon-neutrino, and electron-neutrino spectra for vertical showers at $\theta = 15°$ and $E_{\text{prim}} = 10^{14}$ eV. The left column shows proton-induced showers and the right column shows iron-induced showers. From top to bottom, the rows correspond to $\mu^+ + \mu^-$, $\nu_e + \bar{\nu}_e$, and $\nu_\mu + \bar{\nu}_\mu$. In each panel, the upper plot shows the differential spectrum $\mathrm{d}N/\mathrm{d}E$, where the CORSIKA points represent the mean over 100 showers with its standard error, and the solid line shows the corresponding MCEq calculation. The lower plot shows the ratio CORSIKA/MCEq with the dash line marks unity.

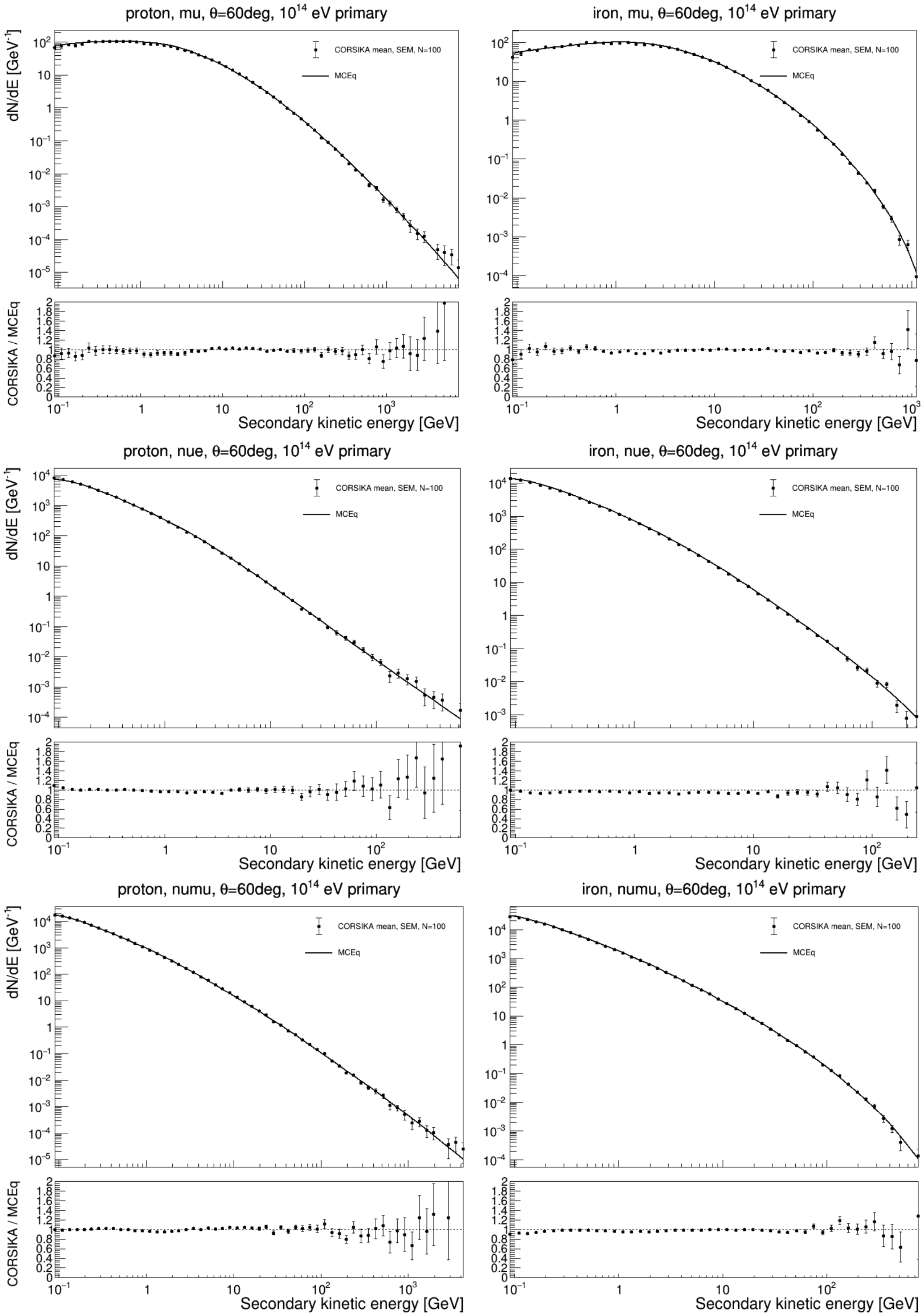

Figure 4.2: CORSIKA-MCEq benchmark of differential muon, muon-neutrino, and electron-neutrino spectra for inclined showers at $\theta = 60^\circ$ and $E_{\text{prim}} = 10^{14}$ eV. The left column shows proton-induced showers and the right column shows iron-induced showers. From top to bottom, the rows correspond to $\mu^+ + \mu^-$, $\nu_e + \bar{\nu}_e$, and $\nu_\mu + \bar{\nu}_\mu$. In each panel, the upper plot shows the differential spectrum $\mathrm{d}N/\mathrm{d}E$, where the CORSIKA points represent the mean over 100 showers with its standard error, and the solid line shows the corresponding MCEq calculation. The lower plot shows the ratio CORSIKA/MCEq with the dash line marks unity.

4.2 Muon-Neutrino Correlation

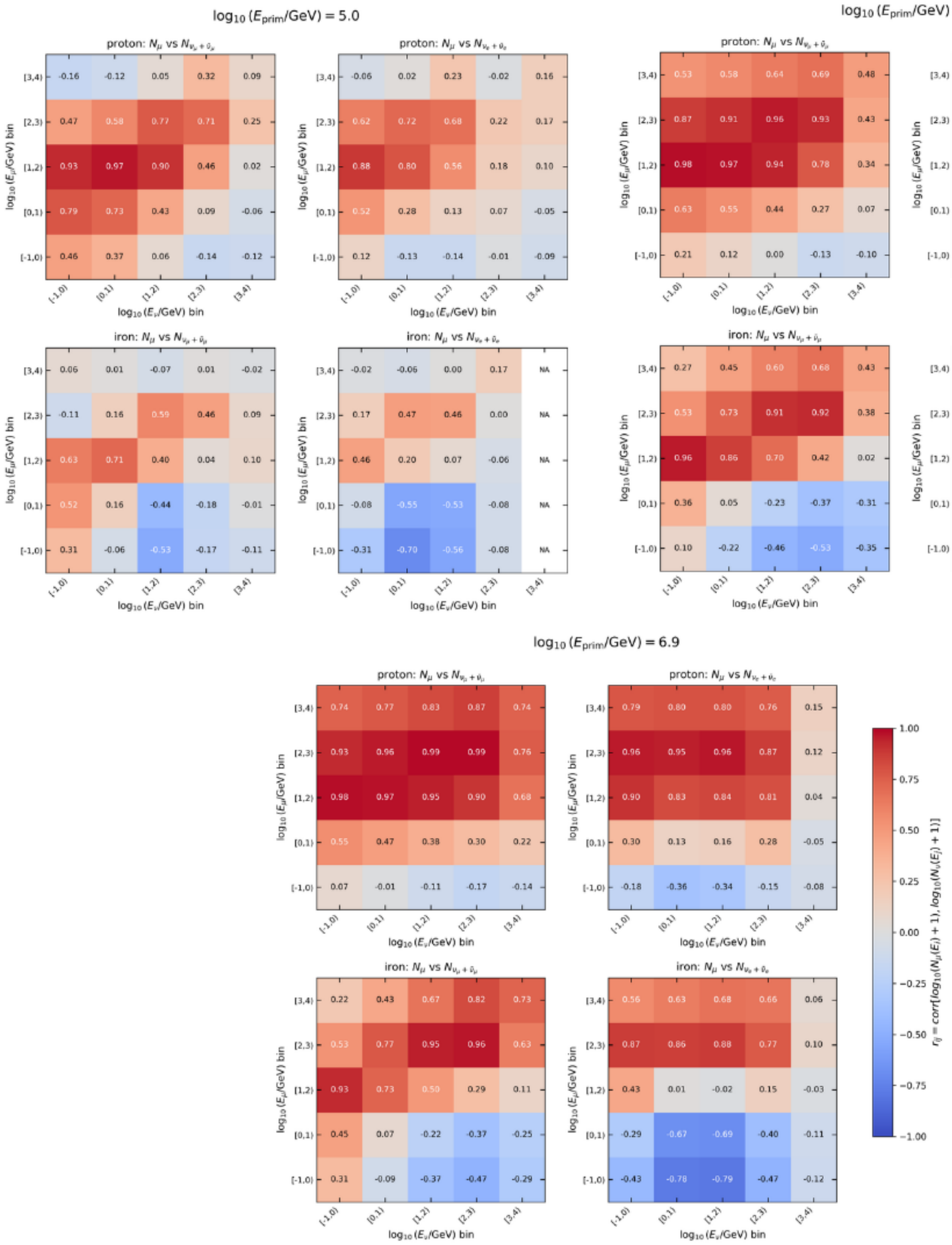

Figure 4.3: Pearson correlation coefficient r between the binned muon multiplicity $N_\mu(E_k)$ and the binned neutrino multiplicities $N_{\nu_\mu+\bar{\nu}_\mu}(E_k)$ and $N_{\nu_e+\bar{\nu}_e}(E_k)$ for proton- and iron-induced CORSIKA showers. The results are shown for three primary energies, $E_{\text{prim}} = 10^5$, 10^6, and $10^{6.9}$ GeV. In each heatmap, the horizontal axis gives the corresponding neutrino kinetic-energy bin. Red colours indicate positive correlation, blue colours indicate negative correlation, and blank cells indicate bins where the correlation could not be evaluated because of insufficient statistics.

To quantify the muon-neutrino correlation shown in the heatmaps and scatter plots, the Pearson coefficient r was calculated for each pair of secondary-energy bins[1].

[1] The secondary-energy bin means the kinetic-energy bins of the secondary muons and neutrinos.

For a given muon-energy bin i and neutrino-energy bin j, each shower k provides a pair of multiplicities

$$x_k = N_{\mu,k}(E_i),$$
$$y_k = N_{\nu,k}(E_j).$$

The Pearson coefficient in each heatmap cell is then

$$r_{ij} = \frac{\sum_{k=1}^{n}(x_k - \bar{x})(y_k - \bar{y})}{\sqrt{\sum_{k=1}^{n}(x_k - \bar{x})^2}\sqrt{\sum_{k=1}^{n}(y_k - \bar{y})^2}}, \tag{4.1}$$

where n is the number of showers used for that bin pair, and $\bar{x}$ and $\bar{y}$ are the corresponding sample means. A value $r_{ij} \simeq 1$ means that showers with more muons in bin i also tend to have more neutrino in bin j. A value near zero means that the two binned multiplicities are weakly related, while a negative value would indicate an anti-correlation.

For each heatmap cell, the Pearson coefficient was calculated only when the corresponding muon-energy bin and neutrino-energy bin contained at least 10 contributing events. Cells not satisfying this requirement were excluded from the correlation map and labelled as NA. This minimum-statistics cut prevents poorly populated bins from producing artificially large or unstable correlation coefficients.

The correlation between N_μ and $N_{\nu_\mu+\bar{\nu}_\mu}$ is generally stronger and more stable than that between N_μ and $N_{\nu_e+\bar{\nu}_e}$. This is expected from the decay chains discussed in **Chapter 2**, section 2.3. Muons and muon-neutrinos are directly connected through charged-pion and charged-kaon decay. Therefore, fluctuations in charged-meson production affect both muons and muon-neutrinos yields at the same time. Electron-neutrinos, however, are mainly produced through the later decay of muons, so their yield also depends on whether the intermediate muon decays before reaching the observation level. This relation weakens and complicates the $N_\mu - N_{\nu_e}$ correlation.

The correlation becomes clearer at higher primary energy. At primary energy bin $E_{\text{prim}} = 10^5$ GeV, some bins show weak or even negative correlations, especially for iron and for high secondary-energy bins. This is mainly a statistical effect due to small number of particles in that secondary-energy bins. At primary energy bin $E_{\text{prim}} = 10^6$ GeV and $E_{\text{prim}} = 10^{6.9}$ GeV, the correlations become stronger over a broader range of energy bins. This is expected because higher-energy showers contain larger numbers of secondary particles, reducing statistical fluctuations and making the underlying physical correlation more visible.

The heatmap representation shows that the muon-neutrino correlation depends strongly on the secondary-energy bins. The correlation is not uniform across the full energy range, which means that the relation between N_μ and N_ν cannot be described only by the total shower multiplicity. Instead, the correlation is strongest in the energy regions where the muons and neutrinos are produced by the same part of the hadronic cascade. By looking at this heatmap, we can select the secondary-energy bins with the highest $N_\mu - N_\nu$ correlations, which is specify for primary masses and energies.

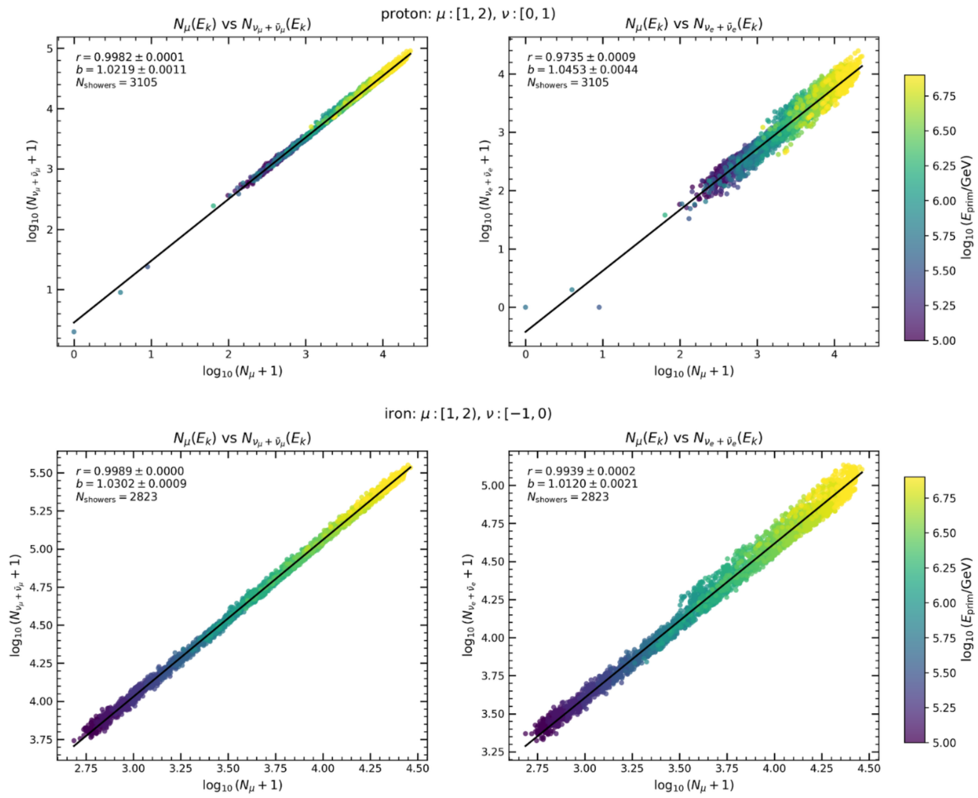

Figure 4.4: Event-by-event correlation between the logarithmic muon count and neutrino count for proton- and iron-induced showers. The upper row shows proton showers, using the identified bin combination $\mu : [1, 2)$ and $\nu : [0, 1)$. The lower row shows iron showers, using the identified bin combination $\mu : [1, 2)$ and $\nu : [-1, 0)$ while the lower panels is iron showers. The left panels show $N_\mu(E_k)$ versus $N_{\nu_\mu+\bar{\nu}_\mu}(E_k)$, while the right panels show $N_\mu(E_k)$ versus $N_{\nu_e+\bar{\nu}_e}(E_k)$. The points are coloured by primary energy, $\log_{10}(E_{\text{prim/GeV}})$. The black line shows a linear fit in logarithmic space, with Pearson coefficient r, fitted slope b, and number of showers N_{shower} reported in each panel.

Follow this idea, we identified the secondary-energy bin with the strongest muon-neutrino correlations and make a scatter plot for all primary energies. The identified optimal bin pairs are $10 < E_\mu < 100$ GeV - $1 < E_\nu < 10$ GeV for proton showers and $10 < E_\mu < 100$ GeV - $0.1 < E_\nu < 1$ GeV for iron showers. The uncertainty in the slope b was obtained from the ordinary least-squares standard error, while the uncertainty in r was estimated using the Fisher z-transformation. These uncertainties represent statistical errors from a finite simulated shower sample.

For $N_\mu - N_{\nu_\mu+\bar{\nu}_\mu}$, the points lie very close to the straight line in logarithmic space, with $r \simeq 0.998 - 0.999$ and fitted slopes near unity. This indicates an almost proportional scaling between the muon and muon-neutrino multiplicities in those identified bins. The $N_\mu - N_{\nu_e+\bar{\nu}_e}$ relation is also strong, but slightly more scattered, with $r \simeq 0.973 - 0.994$. This supports the interpretation that electron-neutrinos remain correlated with muons, but less directly than muon-neutrinos. However, this strong correlations can also be biased to the general increasing trend of secondary particles with the primary energies. Therefore, the scatter plots should not be interpreted as demonstrating an intrinsic event-by-event correlation between muon and neutrino production. Instead, our idea with this scatter plot is to use it as a feature representation of the simulated showers.

The heatmaps identify the most correlated secondary-energy bins at a given primary energy, while the scatter plots show how the selected observables organise showers across primary energy and primary mass. This makes the scatter representation a useful first step toward a future classification framework.

Chapter 5

Conclusion and Further Study

This thesis investigated the correlation between conventional atmospheric muons and neutrinos produced in extensive air showers at the IceCube observation level using CORSIKA simulations. The main results were focused on the two correlation representations: the Pearson-correlation heatmaps and the logarithmic scatter plots of muon and neutrino counts.

The Pearson correlation analysis shows that the muon-neutrino correlation is strongly dependent on the secondary-energy bins. The resulting Pearson correlation coefficients are presented as heatmaps. The $N_\mu - N_{\nu_\mu}$ correlation is generally stronger and more stable than $N_\mu - N_{\nu_e}$ correlation. This behaviour is consistent with charged-pion and charged-kaon decay chains, in which muons and muon-neutrinos are produced directly from the same parent mesons. The heatmaps also show that the optimal correlated energy bins depend on the primary mass. For proton-induced showers, the strongest correlation with a given muon-energy bin tends to appear at a higher neutrino-energy bin than for iron-induced showers. This reflects the different development of the lightest and heaviest primaries, which produce different secondary particle energy distributions. Thus, the heatmaps provide not only a diagnostic of the muon-neutrino connection, but also a compact representation of how primary mass affects the energy structure of the shower.

The scatter plots provide a complementary view of how the muon and neutrino multiplicities scale with the size of the hadronic cascade. Although the strong correlations are largely driven by the common dependence of both observables on primary energy, these scatter plots provide a preliminary feature representation for future classification studies. Future work could investigate whether these correlation structures can be used as the basis of data-driven methods for primary mass classification or air shower characterisation.

Future work could first use IceTop observables to define classes of air-shower events that are nearly model-independent. Such an observable may include, for example,

$$S = (S_{125}, X_{\max}, N_\mu, \theta, ...). \tag{5.1}$$

Events could then be grouped in this observable space using clustering or other unsupervised methods. This would define data-driven shower categories before imposing a specific hadronic interaction model or composition assumption. After these IceTop categories are constructed, one can examine the associated IceCube neutrino observables. These may be represented by a second vector,

$$N = (E_\nu^{\text{reco}}, \theta_\nu^{\text{reco}}, ...), \tag{5.2}$$

where the neutrino-side information may include reconstructed energy, reconstructed direction, or event topology. Mathematically, the future analysis can be formulated through the joint probability of IceTop and IceCube observables under a given physical model M, such as a chosen hadronic-interaction model or primary-composition hypothesis:

$$p(S, N|M) = p(S|M)p(N|S, M). \tag{5.3}$$

Here, $p(S|M)$ describes how the model predicts the distribution of IceTop air-shower observables, while $p(N|S,M)$ describes the conditional neutrino observables expected for a given IceTop event category. The second factor is the key object, it tests whether the neutrino observables associated with an IceTop shower class are consistent with the prediction of a specific physical model.

In other words, the event categories would first be defined from the data structure of IceTop observables, while simulations would be used later to predict or test the conditional neutrino distribution within those categories. If a hadronic-interaction model predicts a conditional distribution $p(N|S,M)$ that does not match the observed IceCube data, then the model would indicate tension with the observed data. This idea is conceptually related to existing IceCube combined-likelihood analyses, where different event samples and event topologies are combined to constrain neutrino flux properties. For example, the IceCube combined maximum-likelihood analysis of the high-energy astrophysical neutrino flux used multiple searches and included shower-like and track-like samples, with fits performed using observables such as energy, zenith angle, and event topology (Aartsen, M. G. and others, 2015).

The results of the present thesis provide the simulation-level motivation for such a study. Overall, this study demonstrates that the correlation between atmospheric muons and neutrinos contains physically meaningful information about air shower development and provides a useful framework for future simulation and detector-level studies. In addition, the CORSIKA simulations were first compared with MCEq using the same physical configuration. Good overall agreement was found between the predicted average muon and neutrino spectra, indicating that the two independent simulation approaches provide a consistent description of the average shower development. In a future detector-level analysis, the CORSIKA muon observables could be replaced by IceTop observable such as S_{125}, zenith angle, and muon-sensitive shower quantities, while the simulated neutrino counts could be replaced by IceCube neutrino observables such as reconstructed energy, direction, and event topology.

The main limitation of this work is the restricted statistical and physical scope of the simulation sample. Future work should therefore increase the number of simulated showers to stabilise the correlation coefficients, especially in the high-energy tails, reduce empty or poorly populated heatmap bins, and apply stratified bootstrap resampling within each primary-energy bin to obtain more robust confidence intervals for r and b. Future simulations should also include intermediate nuclear primaries, such as helium, carbon-nitrogen-oxygen, silicon-group nuclei, and mixed-composition samples. Including intermediate masses would show whether the muon-neutrino feature space changes smoothly with primary mass, and whether it can provide a useful observable that sensitive to the entire cosmic-ray composition. Moreover, future studies should investigate the dependence of the correlation structure on the choice of hadronic interaction models and atmospheric conditions.

References

A. Aab et al. Measurement of the cosmic-ray energy spectrum above 2.5×10^{18} eV using the Pierre Auger Observatory. *Phys. Rev. D*, 102:062005, 2020a. doi: 10.1103/PhysRevD.102.062005.

A. Aab et al. Features of the energy spectrum of cosmic rays above 2.5×10^{18} eV using the Pierre Auger Observatory. *Phys. Rev. Lett.*, 125:121106, 2020b. doi: 10.1103/PhysRevLett.125.121106.

M. G. Aartsen et al. Characterization of the atmospheric muon flux in IceCube. *Astropart. Phys.*, 78:1–27, 2016. doi: 10.1016/j.astropartphys.2016.01.006.

M. G. Aartsen et al. The IceCube neutrino observatory: instrumentation and online systems. *J. Instr.*, 12(03):P03012, 2017.

M.G. Aartsen et al. Cosmic ray spectrum and composition from PeV to EeV using 3 years of data from IceTop and IceCube. *Phys. Rev. D*, 100:082002, 2019.

Aartsen, M. G. and others. A combined maximum-likelihood analysis of the high-energy astrophysical neutrino flux measured with IceCube. *Astrophys. J.*, 809:98, 2015. doi: 10.1088/0004-637X/809/1/98.

R. Abbasi et al. IceTop: The surface component of IceCube. *Nucl. Instrum. Meth. A*, 700: 188–220, 2013. doi: 10.1016/j.nima.2012.10.067.

R. Abbasi et al. Density of GeV muons in air showers measured with IceTop. *Phys. Rev. D*, 106: 032010, 2022.

R. Abbasi et al. Seasonal Variations of the Atmospheric Muon Neutrino Spectrum measured with IceCube. *Eur. Phys. J. C*, 85(12):1368, 2025.

R. U. Abbasi et al. First observation of the greisen–zatsepin–kuzmin suppression. *Physical Review Letters*, 100:101101, 2008. doi: 10.1103/PhysRevLett.100.101101.

R. U. Abbasi et al. The cosmic-ray energy spectrum between 2 PeV and 2 EeV observed with the TALE detector in monocular mode. *Astrophys. J.*, 865:74, 2018.

P. Abreu et al. The energy spectrum of cosmic rays beyond the turn-down around 10^{17} eV as measured with the surface detector of the Pierre Auger Observatory. *Eur. Phys. J. C*, 81, 2021. Pierre Auger Collaboration.

Eun-Joo Ahn, Ralph Engel, Thomas K. Gaisser, Paolo Lipari, and Todor Stanev. Cosmic ray interaction event generator SIBYLL 2.1. *Phys. Rev. D*, 80:094003, 2009. doi: 10.1103/PhysRevD.80.094003.

R. Alfaro et al. All-particle cosmic ray energy spectrum measured by the HAWC experiment from 10 to 500 TeV. *Phys. Rev. D*, 96:122001, 2017. doi: 10.1103/PhysRevD.96.122001.

M. Amenomori et al. The all-particle spectrum of primary cosmic rays in the wide energy range from 10^{14} to 10^{17} eV observed with the Tibet-III air-shower array. *Astrophys. J.*, 678:1165, 2008.

K. Andeen, M. Plum, et al. Cosmic-ray spectrum and composition from PeV to EeV using three years of data from IceTop and IceCube. In *Proceedings of the 36th International Cosmic Ray Conference*, page 172, 2019. IceCube Collaboration.

T. Antoni et al. KASCADE measurements of energy spectra for elemental groups of cosmic rays. *Astropart. Phys.*, 24:1, 2005. doi: 10.1016/j.astropartphys.2005.04.001.

W. D. Apel et al. Kneelike structure in the spectrum of the heavy component of cosmic rays observed with KASCADE-Grande. *Phys. Rev. Lett.*, 107:171104, 2011. doi: 10.1103/PhysRevLett.107.171104.

Francesca Ballarini et al. The FLUKA code: Overview and new developments. *EPJ Nuclear Sci. Technol.*, 10:16, 2024. doi: 10.1051/epjn/2024015.

James J. Beatty, John Matthews, and Scott P. Wakely. Cosmic rays. In *Review of Particle Physics*. Particle Data Group, 2022. Revised October 2021, included in R. L. Workman et al., Prog. Theor. Exp. Phys. 2022, 083C01.

A. Capella, U. Sukhatme, C. I. Tan, and J. Tran Thanh Van. Dual parton model. *Physics Reports*, 236:225–329, 1994.

Nicholas Choma, Federico Monti, Lisa Gerhardt, Tomasz Palczewski, Zahra Ronaghi, Prabhat, Wahid Bhimji, Michael M. Bronstein, Spencer R. Klein, and Joan Bruna. Graph neural networks for IceCube signal classification. *arXiv preprint arXiv:1809.06166*, 2018. doi: 10.48550/arXiv.1809.06166.

L. Durand and H. Pi. QCD and rising cross sections. *Phys. Rev. Lett.*, 58:303, 1987. doi: 10.1103/PhysRevLett.58.303.

Anatoli Fedynitch, Julia Becker Tjus, and Paolo Desiati. Influence of hadronic interaction models and the cosmic-ray spectrum on the high-energy atmospheric muon and neutrino flux. *Phys. Rev. D*, 86:114024, 2012. doi: 10.1103/PhysRevD.86.114024.

Anatoli Fedynitch, Ralph Engel, Thomas K. Gaisser, Felix Riehn, and Todor Stanev. Calculation of conventional and prompt lepton fluxes at very high energy. In *EPJ Web of Conferences*, volume 99, page 08001, 2015. doi: 10.1051/epjconf/20159908001.

A. Ferrari and P. R. Sala. A new model for hadronic interactions at intermediate energies for the FLUKA code. In P. Dragovitsch, S. L. Linn, and M. Burbank, editors, *Proc. MC93 Int. Conf. on Monte Carlo Simulation in High Energy and Nuclear Physics, Tallahassee (Florida), 22–26 February 1993*, pages 277–288, Singapore, 1994. World Scientific.

A. Ferrari, P. R. Sala, A. Fassò, and J. Ranft. FLUKA: A multi-particle transport code. Technical Report CERN-2005-010, SLAC-R-773, INFN-TC-05-11, CERN INFN SLAC, October 2005.

R. S. Fletcher, T. K. Gaisser, Paolo Lipari, and Todor Stanev. SIBYLL: An event generator for simulation of high-energy cosmic ray cascades. *Phys. Rev. D*, 50:5710–5731, 1994.

Yu. A. Fomin et al. Cosmic-ray energy spectrum measurement with the MSU air-shower array. In *Proceedings of the 22nd International Cosmic Ray Conference*, volume 2, page 85, Dublin, 1991.

E. Gadioli and P. Hodgson. *Pre-equilibrium Nuclear Reactions*. Clarendon Press, 1992.

T. K. Gaisser and F. Halzen. "soft" hard scattering in the TeV range. *Phys. Rev. Lett.*, 54:1754, 1985. doi: 10.1103/PhysRevLett.54.1754.

Thomas K. Gaisser. *Cosmic Rays and Particle Physics*. Cambridge University Press, Cambridge, United Kingdom, 1 edition, 1990. ISBN 0-521-33931-6.

Thomas K. Gaisser, Ralph Engel, and Elisa Resconi. *Cosmic Rays and Particle Physics*. Cambridge University Press, Cambridge, United Kingdom, 2 edition, 2016. ISBN 978-0-521-01646-9. doi: 10.1017/CBO9781139192194.

M. A. K. Glasmacher et al. The cosmic-ray energy spectrum between 10^{14} and 10^{16} eV. *Astropart. Phys.*, 10:291, 1999.

R. Glauber. *Lectures in Theoretical Physics*, volume 1. Interscience, New York, London, 1959.

R. J. Glauber. Cross-sections in deuterium at high-energies. *Phys. Rev.*, 100:242, 1955. doi: 10.1103/PhysRev.100.242.

R. J. Glauber and G. Matthiae. High-energy scattering of protons by nuclei. *Nucl. Phys. B*, 21: 135–157, 1970. doi: 10.1016/0550-3213(70)90511-0.

M. L. Good and W. D. Walker. Diffraction dissociation of beam particles. *Phys. Rev.*, 120: 1857–1860, 1960. doi: 10.1103/PhysRev.120.1857.

J. J. Griffin. Statistical model of intermediate structure. *Phys. Rev. Lett.*, 17:478, 1966. doi: 10.1103/PhysRevLett.17.478.

Francis Halzen and Dan Hooper. High-energy neutrino astronomy: The cosmic ray connection. *Reports on Progress in Physics*, 65:1025–1078, 2002. doi: 10.1088/0034-4885/65/7/201.

D. Heck, J. Knapp, J. N. Capdevielle, G. Schatz, and T. Thouw. CORSIKA: A monte carlo code to simulate extensive air showers. Technical Report FZKA 6019, Forschungszentrum Karlsruhe, Karlsruhe, Germany, 1998.

D. Heck, T. Hüge, and T. Pierog. *Extensive Air Shower Simulation with CORSIKA: A User's Guide*. Karlsruhe Institute of Technology, Karlsruhe, Germany, 2025.

D. Ivanov et al. Telescope array cosmic-ray energy spectrum measurement. In *Proceedings of the 36th International Cosmic Ray Conference*, page 298, 2019. Telescope Array Collaboration.

Donghwa Kang. Cosmic ray physics with IceCube and IceTop. Space and Cosmic Ray Physics Seminar, University of Maryland, November 2022. 7 November 2022.

Donghwa Kang. Recent results of cosmic-ray studies with IceTop at the IceCube neutrino observatory. *Advances in Space Research*, 72:4613–4624, 2023. doi: 10.1016/j.asr.2023.09.027. On behalf of the IceCube Collaboration.

Donghwa Kang. Detection of cosmic rays from PeV to EeV. Presentation at the 2025 Fall Meeting of the Korean Space Science Society, October 2025. 29 October 2025.

Donghwa Kang and Andreas Haungs. The cosmic-ray spectrum in the PeV to EeV energy range. *Advances in Space Research*, 74(9):4403–4408, 2024. doi: 10.1016/j.asr.2024.06.053.

A. A. Lagutin, A. V. Plyasheshnikov, and V. V. Uchaikin, 1979. Proc. 16^{th} Int. Cosmic Ray Conf., Kyoto (Japan), **7** (1979) 18; J. N. Capdevielle and J. Gawin, J. Phys. G: Nucl. Part. Phys. **8** (1982) 1317; J. N. Capdevielle, KASCADE Collaboration, Proc. 22^{nd} Int. Cosmic Ray Conf., Dublin (Ireland), **4** (1991) 405.

J. Matthews. A Heitler model of extensive air showers. *Astropart. Phys.*, 22:387–397, 2005. doi: 10.1016/j.astropartphys.2004.09.003.

C. Meurer, J. Blümer, R. Engel, A. Haungs, and M. Roth. Muon production in extensive air showers and its relation to hadronic interactions. *Czechoslovak Journal of Physics*, 56:A211, 2006. doi: 10.1007/s10582-006-0156-9.

M. Nagano et al. Energy spectrum of primary cosmic rays between $10^{14.5}$ and 10^{18} eV. *Journal of Physics G: Nuclear Physics*, 10:1295, 1984.

Walter R. Nelson and Yoshihito Namito. The EGS4 Code System: Solution of Gamma-Ray and Electron Transport Problems. In *Proceedings of the International Conference on Supercomputing in Nuclear Applications*, Mito City, Japan, March 1990. SLAC-PUB-5193.

Walter R. Nelson, Hideo Hirayama, and David W. O. Rogers. The EGS4 Code System. Technical Report SLAC-265, Stanford Linear Accelerator Center, Stanford, California, December 1985.

Hector A. Ortiz, Jose Bellido, Rolando Perca, Ronald Pastor, and Luis Otiniano. A study of the number of muons in air showers at the detector level at energies around 1 tev. In *Proceedings of the 38th International Cosmic Ray Conference (ICRC2023)*, volume ICRC2023 of *Proceedings of Science*, page 437, 2023. doi: 10.22323/1.444.0437.

G. Pancheri and Y. N. Srivastava. Jets in minimum bias physics. *Phys. Lett. B*, 159:69, 1985.

G. Pancheri and Y. N. Srivastava. Low p_T jets and the rise with energy of the inelastic cross-section. *Phys. Lett. B*, 182:199–207, 1986.

F. Riehn, R. Engel, A. Fedynitch, T. K. Gaisser, and T. Stanev. A new version of the event generator sibyll. In *Proceedings of Science*, PoS ICRC2015, page 558, 2016.

Felix Riehn, Ralph Engel, Anatoli Fedynitch, Thomas K. Gaisser, and Todor Stanev. Hadronic interaction model SIBYLL 2.3d and extensive air showers. *Phys. Rev. D*, 102:063002, 2020.

T. Sjostrand. Status of fragmentation models. *Int. J. Mod. Phys. A*, 3:751, 1988.

V. Weisskopf. Statistics and nuclear reactions. *Phys. Rev.*, 52:295, 1937. doi: 10.1103/PhysRev. 52.295.

Appendix A

Additional Materials

A.1 Hadronic Interaction Models

A.1.1 Comparison between Hadronic Interaction Models

Table A.1: Comparison of the hadronic interaction models mentioned in this work. SIBYLL, EPOS, and QGSJET describe high-energy interactions, whereas FLUKA and GHEISHA describe the lower-energy stages of air-shower development. Based on the *CORSIKA 7.8050 User's Guide* (Heck et al., 2025).

Model	Energy regime and approach	Main distinction and relevance to air showers
SIBYLL	High-energy model based on QCD minijet production, multiple parton scattering, and string fragmentation.	Designed as a computationally efficient event generator for cosmic-ray cascades. Its treatment of forward particles, leading hadrons, baryons, and mesons affects energy transport through the cascade, the depth of shower maximum, and atmospheric muon and neutrino production.
EPOS	High-energy model based on Gribov-Regge theory, multiple scattering, remnant excitation, and collective hadronisation.	Provides a detailed treatment of hadron-nucleus and nucleus-nucleus interactions. Its description of remnants, baryons, and strange-particle production can produce different secondary multiplicities and muon yields from other high-energy models.
QGSJET	High-energy model based on Reggeon Field Theory, multiple Pomeron exchanges, and quark-gluon string formation.	Emphasises multiple-scattering and nonlinear-screening effects at very high energies. It influences hadronic cross-sections, inelasticity, secondary multiplicity, shower-development depth, and the resulting muon component.
FLUKA	Low-energy model based on microscopic hadron-nucleus transport. Its PEANUT framework includes an intranuclear cascade, pre-equilibrium emission, evaporation, fragmentation, and nuclear de-excitation.	Provides a detailed description of nuclear-medium effects and conservation laws. FLUKA is used as the low-energy hadronic model in this thesis. It controls the later cascade generations and the production and transport of low-energy pions, kaons, and nucleons.
GHEISHA	Low-energy model based mainly on phenomenological and empirical parameterisations of hadron-nucleus interactions.	Calculates elastic and inelastic hadronic cross-sections, interactions, and secondary-particle production in air below approximately 80 GeV. It is an older and less microscopically detailed model than FLUKA. Differences in particle-production spectra, interaction kinematics, and energy conservation can affect the predicted low-energy hadronic and ground-level muon components.

The models used for the CORSIKA simulations of EAS in this work will be discussed in greater detail in the following subsections.

A.1.2 High-Energy Hadronic Interaction Model: SIBYLL 2.3

SIBYLL (Fletcher et al., 1994) is a high-energy hadronic interaction event generator developed for MC simulations of cosmic-ray cascades in the atmosphere. It is designed as an efficient generator for ultra-high-energy interactions, aiming of treating hadron-hadron, hadron-nucleus, and nucleus-nucleus interactions within one efficient framework. The motivation was due to earlier air-shower generators often used simple parameterisations of accelerator data, whereas increasingly sophisticated air-shower experiments required more detailed description of hadronic interactions and their extrapolation beyond measured energies. SIBYLL was therefore targeted to reproduce the experimentally observed features of accelerator interactions while remaining computational efficient for cascade simulations.

The principal physics goal of SIBYLL is to model those parts of hadronic interactions that most strongly control cascade development, including the fragmentation region, minijet production, and the treatment of hadron-nucleus and nucleus-nucleus interactions relevant to air-shower development. The first SIBYLL model (Fletcher et al., 1994), usually referred to as SIBYLL 1.7, was built based on the Dual Parton Model (Capella et al., 1994) for soft colour string production and the minijet model (Gaisser and Halzen, 1985, Pancheri and Srivastava, 1985, 1986, Durand and Pi, 1987) for hard parton scattering, combined with final-state hadronisation described through the Lund string fragmentation (Sjostrand, 1988).

At low energy, the model represents a non-diffractive interaction between hadrons through colour exchange between quarks and diquarks, followed by the fragmentation of colour strings into hadrons (Fletcher et al., 1994, Sjostrand, 1988). The initial energy fraction x of a quark or diquark fragment that forms the string end, was sampled in the original formulation as

$$f_q(x) = \frac{(1-x)^\alpha}{[x^2 + \mu^2/s]^{1/4}}, \tag{A.1}$$

with $\mu = 0.35$ GeV and $\alpha = 30$ for the proton case (Fletcher et al., 1994). Then, according to the Lund fragmentation function, the fractional energy z of each hadron produced during the subsequent fragmentation of that string, is generated as this function

$$f(z) = \frac{(1-z)^\alpha}{z} \times e^{\frac{-b\, m_T^2}{z}}, \tag{A.2}$$

where $\alpha = 0.5$, $b = 0.8$, and m_T is the transverse mass of the produced hadron (Fletcher et al., 1994). This fragmentation formula determines how energy is shared among secondary hadrons.

At high energy, the model adds the production of minijets, which are jets with low transverse momentum produced by interactions between partons (Fletcher et al., 1994, Gaisser and Halzen, 1985, Pancheri and Srivastava, 1985, 1986, Durand and Pi, 1987). Soft string fragmentation mainly describes low momentum transfer interactions and approximately scaling forward spectra, so it cannot generate the observed energy dependent rise of central particle density, charged multiplicity, transverse momentum and inelastic cross section. For this reason, minijet component was introduced and supplied this missing high-energy component by allowing multiple hard parton scattering in one hadronic collision.

The probability of hard interactions is treated in impact parameter space. In the original formulation, the average number of hard interactions at impact parameter b and squared centre of mass energy s is written as

$$n(b,s) = A(b)\sigma_{\text{QCD}}(s), \tag{A.3}$$

where $A(b)$ is the overlap function of the colliding hadrons and σ_{QCD} is the inclusive hard parton cross section (Fletcher et al., 1994).

The inelastic cross section is then obtained from the eikonal expression (Good and Walker, 1960)

$$\sigma_{inel} = \int d^2b[1 - e^{-2\chi(b,s)}], \tag{A.4}$$

which allows several interactions to occur in one collision while preserving unitarity (Fletcher et al., 1994). This equation describes the probability of an inelastic hadron-hadron interaction at a given impact parameter, but an air shower target is a nucleus containing many nucleons. Therefore, the interactions of hadrons with nuclei can be described with the Glauber theory (Glauber and Matthiae, 1970), where the collision probability depends on the impact parameter and on the distribution of nucleons inside the target nucleus. Interactions between nuclei are treated through a semi-superposition method, in which the interaction of the projectile nucleus is built from interactions of its nucleons with the target nucleus.

Since the first version was released in 1994, the SIBYLL model has been modified and retuned in successive versions to incorporate new accelerator measurements, improve the treatment of soft and hard particle production, refine diffraction and nuclear interaction, and reduce uncertainties in EAS predictions and inclusive lepton flux calculations. These developments led to the post-LHC SIBYLL 2.3 series, in which the original minijet and string fragmentation framework is retained but updated with improved descriptions of cross sections, baryon production, and charm particle production (Riehn et al., 2016).

SIBYLL 2.3d (Riehn et al., 2020) is one of the later refinements in the SIBYLL 2.3 series, in which leading baryons are described through an excited remnant mechanism rather than only through a tuned leading fragmentation function. This is important because leading particles carry a large fraction of the projectile energy and transport energy deeper into the atmosphere. The production of muons is strongly affected by the treatment of leading mesons and baryons. A neutral pion transfers energy to the electromagnetic cascade through neutral pion decay, whereas a neutral rho meson keeps energy in the hadronic cascade through $\rho^0 \rightarrow \pi^+ + \pi^-$. Therefore, enhanced production of leading ρ^0 mesons increases the number of charged pions that can later decay into muons and neutrinos. Baryon and antibaryon production also increases the muon content because baryons continue to interact through several cascade generations before their energy falls below the particle production threshold. In the Heitler-Matthews approximation (Matthews, 2005), the mean number of muons can be written as

$$N_\mu = \left(\frac{E_0}{E_c}\right)^\alpha, \quad \alpha = \frac{\ln(n_{ch})}{\ln(n_{tot})}, \tag{A.5}$$

where E_0 is the primary energy, E_c is a critical energy below which charged pions predominantly decay rather than continue the hadronic cascade, n_{ch} is the charged multiplicity and n_{tot} is the total multiplicity (Ahn et al., 2009). From this expression, any change in the charged fraction of the hadronic cascade can change the muon yield. Compared with earlier versions, SIBYLL 2.3d predicts an increased muon content and changes in the predicted depth of shower maximum due to its updated treatment of forward particle production, remnant excitation, and hadronic interactions.

In this thesis, SIBYLL 2.3d is used as the high-energy hadronic interaction model in the CORSIKA simulations for the main analysis. For the benchmark work, we used the latest version SIBYLL 2.3e. The differences between SIBYLL 2.3d and 2.3e are expected to have negligible impact on the observables considered in this benchmark work. The documents discussed here attempt to give a detailed description of the physics behind the SIBYLL models.

A.1.3 Low-Energy Hadronic Interaction Model: FLUKA

FLUKA (Ferrari et al., 2005) is a general-purpose MC code for calculations of particle transport and interactions in matter. Its design philosophy is to build a model follows accurate physics frameworks, rather than prioritise mathematical shortcuts and computational efficiency. FLUKA use microscopic physics models wherever possible, enforce consistency and conservation laws at each reaction step and across all reaction types, and validate the results at individual collisions or reactions, the most fundamental level possible (Ferrari et al., 2005). In this work, it is used through CORSIKA only as the low-energy hadronic interaction model to describe secondary hadron production in extensive air shower simulations. In this role, FLUKA calculates inelastic hadron cross sections with air nuclei and performs the corresponding interactions and secondary particles production, including de-excitation of the target nucleus

At the hadron-nucleon level, FLUKA uses different physics descriptions depending on energy. Below a few GeV, FLUKA describes inelastic interactions by hadronic resonances production and decay. At higher energies, FLUKA adopts a Dual Parton Model (DPM) Capella et al. (1994) description of hadron-nucleon interaction, where the collision produces colour strings that subsequently hadronise into final-state particles. For the low-energy hadronic interaction simulations, we focus on the low- and intermediate-energy treatment of hadron-nucleus interactions, since secondary particles in an air shower interact mainly with nitrogen and oxygen nuclei.

In hadron-nucleus level, the central model is PEANUT (Ferrari and Sala, 1994). PEANUT was originally designed to simulate interactions of nucleons, pions and photons with nuclei from about 2 GeV down to the reaction threshold, or down to 20 MeV for neutrons (Ballarini et al., 2024). The hadron-nucleus interaction is modelled through a sequence of physical stages. At sufficiently high projectile energy, the Glauber-Gribov model (Glauber, 1955, 1959) describes the possibility that the projectile interacts with several nucleons in the target nucleus. This is followed by a GINC (Griffin, 1966, Gadioli and Hodgson, 1992), in which the incoming hadron and the produced secondary particles propagate through the nuclear medium and may interact again before leaving the nucleus. The cascade is then coupled to a statistical pre-equilibrium stage, followed by evaporation or fragmentation of the excited remnant, and finally, gamma de-excitation. Some stages, may be omitted depending on the projectile energy, for example, nucleons below a few tens of MeV may enter the pre-equilibrium treatment directly (Ballarini et al., 2024).

The intra-nuclear cascade is the most intuitive part of PEANUT for air-shower physics. In this stage, a secondary hadron entering an air nucleus can collide with a bound nucleon, produce other particles, and those particles may continue to propagate and interact inside the same nucleus. FLUKA treats these particles along semi-classical trajectories affected by nuclear and Coulomb potentials, so refraction and reflection at the nuclear surface are included (Ballarini et al., 2024). The target nucleus is represented by density distributions, and the interaction probability depends on the local nuclear density and on free space hadron-nucleon cross sections corrected for nuclear-medium effects, such as Fermi motion. The local Fermi momentum is written as

$$k_F(r) = \left(\frac{3\pi^2}{2}\rho(r)\right)^{1/3}, \tag{A.6}$$

where $\rho(r)$ is the local nuclear density (Ballarini et al., 2024, p. 6). Therefore, the maximum momentum of nucleons inside the nucleus depends on the local density, denser regions correspond to larger Fermi momenta. Since a hadron may collide with a moving bound nucleon rather than a stationary one, Fermi motion modifies the effective collision energy and the angular distribution of the produced secondaries.

FLUKA also includes quantum effects that prevent the cascade from becoming an unrealistic sequence of independent free-particle collisions. Pauli blocking forbids final-state nucleons from occupying already filled nuclear levels, reducing the number of allowed secondary interactions (Ballarini et al., 2024). Formation-zone effects account for the fact that a newly produced fast hadron does not immediately behave as a fully formed particle able to re-interact. The formation time is estimated from the uncertainty principle as

$$\bar{t} = \Delta t \simeq \frac{\hbar}{E_T} = \frac{\hbar}{\sqrt{p_T^2 + M^2}}, \tag{A.7}$$

where M is the secondary-particle mass and p_T is its transverse momentum (Ballarini et al., 2024, p. 6). In the laboratory frame, this becomes

$$t_{lab} = \frac{\hbar E_{lab}}{p_T^2 + M^2}. \tag{A.8}$$

Physically, a high-energy secondary may travel a finite distance before it can re-interact, and if this distance is comparable to or larger than the nuclear radius, the particle can escape the nucleus instead of producing additional intra-nuclear interactions.

After the last cascade, the remaining nucleus is usually excited but not yet fully equilibrated. PEANUT therefore includes a pre-equilibrium stage, which describes the transition from the direct cascade remnant to thermalised compound nucleus. In the exciton model (Griffin, 1966, Gadioli and Hodgson, 1992), this intermediate nuclear configuration is represented by particle-like excitons above the Fermi sea and hole-like excitons below it,

$$n = n_p + n_h, \tag{A.9}$$

where n_p is the number of excited particles and n_h is the number of holes left in the nuclear Fermi sea (Ballarini et al., 2024, p. 10). The quantity n tracks the degree of internal redistribution of the excitation energy. As nucleon-nucleon collisions proceed, the exciton number increases, and the system approaches statistical equilibrium. The pre-equilibrium chain stops when n becomes sufficiently large or when the excitation energy is below the particle-emission threshold.

Once the residual nucleus is equilibrated, FLUKA treats its de-excitation through evaporation, fission, fragmentation or Fermi break-up, followed by gamma de-excitation (Ballarini et al., 2024). In the evaporation stage (Weisskopf, 1937), the excited nucleus behaves like a hot system that loses energy by emitting nucleons or light fragments. The nuclear state-density dependence is given as

$$\rho(U) \propto \frac{e^{2\sqrt{aU}}}{U^{5/4}}, \tag{A.10}$$

where U is the excitation energy and a is the level-density parameter (Ballarini et al., 2024, p. 11), this nuclear level density controlled the emission probability in the evaporation stage.

For the present thesis, FLUKA is used to control how secondary pions, kaons, nucleons and antinucleons interact with air nuclei after the high-energy shower development has already begun. These interactions affect whether secondary mesons re-interact, are absorbed, or survive long enough to decay. This is particularly important because the competition between interaction and decay determines the production of conventional atmospheric muons and neutrinos. The main physics of involved processes has been summarised in this subsection.

A.1.4 Electromagnetic Interaction Model: EGS4+LPM

EGS4 (Nelson et al., 1985), the Electron-Gamma Shower code system, is a general-purpose MC package for the coupled transport of electrons, positrons, and photons, with energy range extending from a few keV to several TeV. In this work, the EGS4 package with the LPM option is used in CORSIKA to simulate the electromagnetic component of the EAS.

The physical basis of EGS4 is the stochastic development of an electromagnetic cascade through repeated radiation and conversion processes. Electrons and positrons lose energy by collision processes, which excite or ionise atoms, and by radiative bremsstrahlung, which produces secondary photons (Nelson et al., 1985). At low electron energy, collisional energy loss dominates, whereas at high electron energy bremsstrahlung becomes dominant, the approximate transition of this occurs near the critical energy of the medium (Nelson et al., 1985). High-energy photons then convert mainly into electron-positron pairs, while Compton scattering and the photoelectric effect become more important at lower photon energies (Nelson et al., 1985). The process of $e^\pm \to e^\pm + \gamma$ and $\gamma \to e^+ + e^-$ is therefore the main mechanism that increases the number of electromagnetic particles while reducing their mean energy as the shower develops.

In EGS4, electrons and positrons are transported with bremsstrahlung production, positron annihilation, Bhabha scattering, Møller scattering, continuous energy loss and multiple Coulomb scattering according to Molière theory (Nelson and Namito, 1990). Photons are transported with pair production, Compton scattering and the photoelectric effect, while coherent Rayleigh scattering is available as a non-default option (Nelson and Namito, 1990). Continuous charged-particle energy loss is composed of soft bremsstrahlung and collisional loss terms, and the collisional part is evaluated using the restricted Bethe-Bloch stopping power with the Sternheimer density-effect correction (Nelson and Namito, 1990). The continuous energy loss between discrete interactions can be written as

$$-\left(\frac{\mathrm{d}E_\pm}{\mathrm{d}x}\right)_{\text{total}} = -\left(\frac{\mathrm{d}E_\pm}{\mathrm{d}x}\right)_{\text{soft, bremsstrahlung}} - \left(\frac{\mathrm{d}E_\pm}{\mathrm{d}x}\right)_{\text{Sub-Cutoff, Atomic Electrons}} . \tag{A.11}$$

where $\pm$ denotes positive or negative electrons (Nelson et al., 1985, p. 66). The first term describes bremsstrahlung photons below the photon transport threshold, while second term describes energy transferred to atomic electrons without producing explicitly transported secondary electrons.

The transport is governed by interaction probabilities derived from cross sections. For a particle in a medium with molecular weight M, density ρ, Avogadro constant N_A, and total cross-section

σ_t, the mean free path (Nelson et al., 1985, p. 14) is

$$\lambda = \frac{M}{N_A \rho \sigma_t}. \tag{A.12}$$

The probability for an interaction in an infinitesimal path length dx (Nelson et al., 1985, p. 14) is therefore

$$P_r\{\text{interaction in distance dx}\} = \frac{\mathrm{d}x}{\lambda}. \tag{A.13}$$

The number of mean free paths to next interaction is sampled

$$N_\lambda = -\ln \xi, \tag{A.14}$$

where ξ is a uniformly distributed random number (Nelson et al., 1985, p. 14), so that interaction points are generated according to the exponential attenuation law. After a real interaction point is reached, the interaction channel i is selected from its branching ratio,

$$P_i = \frac{\sigma_i}{\sigma_t}, \quad F(i) = \sum_{j=1}^{i} \frac{\sigma_j}{\sigma_t}, \tag{A.15}$$

where σ_i is the cross-section of process i and $\sigma_t = \sum_i \sigma_i$ (Nelson et al., 1985). This procedure links the microscopic cross-sections of bremsstrahlung, pair production, Compton scattering and charged-particle interactions to the macroscopic development of the simulated electromagnetic cascade.

A key distinction in EGS4 is the treatment of discrete and continuous charged-particle interactions. Photon interactions have sufficiently small cross-sections that pair production, Compton scattering and photoelectric absorption can be simulated as explicit events, so photons travel in straight lines with constant energy between interactions (Nelson et al., 1985). For electrons and positrons, many low-momentum-transfer interactions have very large cross-sections, so EGS4 does not simulate every microscopic scattering or soft energy-loss event individually (Nelson et al., 1985). Instead, the cutoff parameters AE and AP separate discrete events from continuous transport: an electron interaction producing a delta ray with total energy at least AE, or a photon with energy at least AP, is treated discretely, while softer interactions contribute to continuous energy loss and angular deflection (Nelson et al., 1985). This treatment is essential for air-shower simulations because it preserves the stochastic structure of hard electromagnetic interactions without making the calculation prohibitively expensive.

At high energies, bremsstrahlung and pair production are suppressed by the LPM effect. The suppression occurs because the formation length of these electromagnetic interactions becomes comparable to the spacing between scattering centres in the medium. As a result, the interaction lengths for bremsstrahlung and pair production increase, delaying the development of the electromagnetic cascade and shifting the shower maximum deeper into the atmosphere. Thus, the LPM option in CORSIKA enables this suppression within the EGS4 electromagnetic transport.

A.2 CORSIKA

A.2.1 CORSIKA Input Setup

Table A.2: Main CORSIKA input steering cards

Card	Defines	Setup
RUNNR	Run number used to identify the simulation and to form the output-file name.	Unique run number nnnnnn for each CORSIKA input file.
SEED	Random-number generator initialisation.	Independent seeds were assigned to each run to avoid repeating identical showers.
NSHOW	Number of showers generated in one run.	According to user (typically 1).
PRMPAR	Primary particle, specified by the CORSIKA particle code.	14 for proton and 5626 for iron.
ERANGE	Lower and upper limits of the primary energy in GeV.	Energy bins covering the selected primary-energy range. Equal limits correspond to a fixed primary energy.
THETAP	Lower and upper limits of the primary zenith angle in degrees.	Random-angle simulations used a zenith range; Equal limits give a fixed zenith angle.
PHIP	Lower and upper limits of the primary azimuth angle in degrees.	Uniform azimuthal range, typically 0.0 359.99.
OBSLEV	Observation level in cm above sea level. Particles crossing this level are written to the output.	2840.E2, corresponding to 2840 m, the IceCube/IceTop observation level.
ATMOD	Atmospheric model used for the shower propagation.	33, corresponding to the South Pole April atmosphere used for IceCube-related simulations.
SIBYLL	Activates the SIBYLL high-energy hadronic interaction model selected at compilation.	T (True) means enabled. F (False) means disabled
SIBSIG	Activates the SIBYLL hadronic cross-section treatment.	T (True) means enabled. F (False) means disabled
ELMFLG	Electromagnetic-interaction flags controlling the NKG and EGS4 electromagnetic treatments.	F for NKG and T for EGS4.
ECUTS	Kinetic-energy thresholds for hadrons, muons, electrons, and photons, respectively, in GeV.	0.0500 0.0500 0.0100 0.0020.
LONGI	Longitudinal shower-profile output, including the sampling step and fit/output flags.	Enabled to obtain longitudinal shower information such as $X_{\max}$.
DIRECT	Directory in which the CORSIKA output files are written.	Output path specified for each simulation batch.
USER	User label written to the CORSIKA output metadata.	User-specific identifier.
EXIT	End of the CORSIKA input steering file.	Last card in each input file.

A.3 Analysis

A.3.1 Average Muon and Neutrino Yields

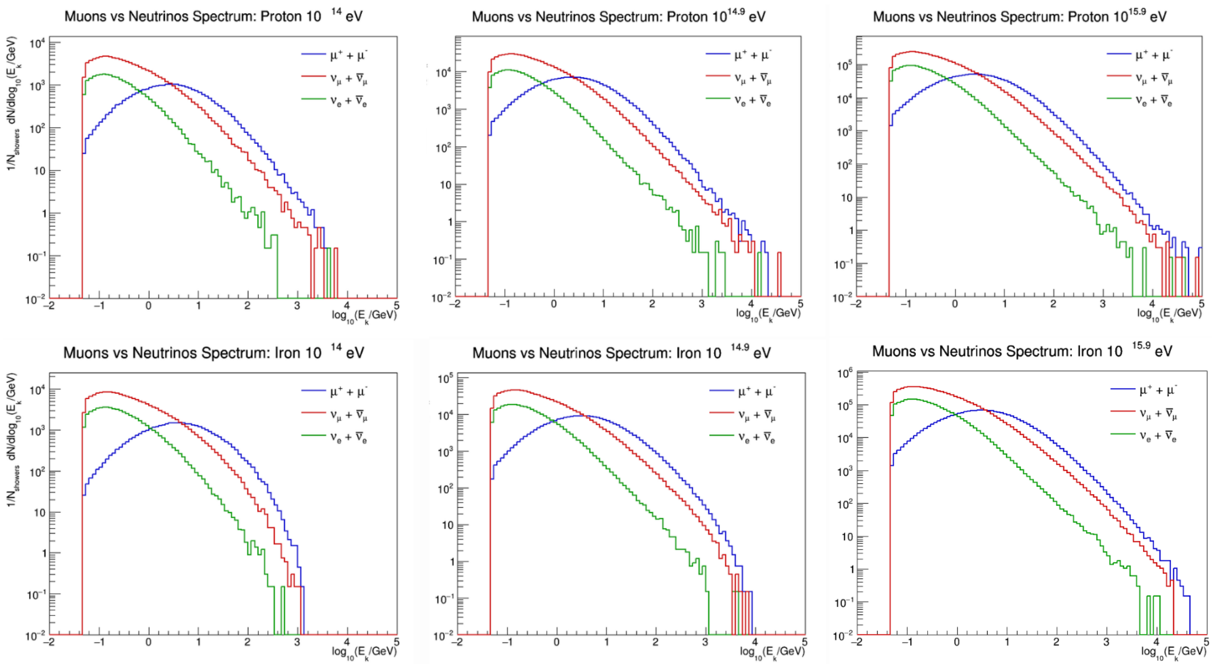

Figure A.1: Average kinetic-energy spectra of conventional muons, muon-neutrinos, and electron-neutrinos at IceCube observation level for CORSIKA proton- and iron-induced air showers.The upper panels show proton primaries and the lower panels show iron primaries, for primary energies 10^{14}, $10^{14.9}$, and $10^{15.9}$ eV. The spectra are normalised by the number of simulated showers $1/N_{\text{shower}}$, showing the average particle yield per shower per logarithmic kinetic-energy interval.

The plotted quantity is

$$\frac{1}{N_{\text{shower}}} \frac{\mathrm{d}N}{\mathrm{d}\log_{10}(E_k/\text{GeV})}, \tag{A.16}$$

where N_{shower} is the number of simulated showers and E_k is the kinetic energy of the secondary particles. Since the secondary kinetic energy spans several orders of magnitude, the spectra are presented per logarithmic energy interval, $\mathrm{d}\log_{10}(E_k/\text{GeV})$.

The first general feature is the increase of all spectra with primary energy. For both proton and iron showers, the yields of $\mu^+ + \mu^-$, $\nu_\mu + \bar{\nu}_\mu$, and $\nu_e + \bar{\nu}_e$ increase from 10^{14} to $10^{15.9}$ eV. This follows directly from the physics of hadronic cascade, where the higher primary energy equivalent to the larger energy available for secondary-particle production. A higher-energy primary produces more secondary pions, kaons, and nucleons; charged pions and kaons then decay into muons and neutrinos. The tails of higher-primary-energy spectra also extend longer to larger E_k, indicating that more energetic primaries can populate rarer high-energy secondary particles.

The second feature is muon spectra extend further towards higher kinetic energy than the neutrino spectra. This is expected from two-body meson-decay kinematics that had been discussed in the **Section 2.3**. In charged pion and charged kaon decay, the muon carries a larger fraction of the pion energy than the accompanying muon neutrinos. Consequently, the muon spectrum extends to higher energies. In addition, high-energy muons are also more likely to survive to the observation level before decaying. The muon spectrum is therefore a combined results of decay kinematics and muon survival.

The neutrino yield exceeds the muon yield in the low-secondary-energy region is also an important feature. This can be explained directly from the conventional muon production in the hadronic cascade previously discussed in the theoretical background. Low-energy muons are likely to decay or lose energy by ionisation before reaching the observation level. Neutrinos, in contrast, are neutral and weakly interacting, so once they are produced they propagate essentially without attenuation to the observation level. Low-energy pion, kaon, and muon decays therefore contribute efficiently to the low-energy neutrino population, while the corresponding low-energy muon population is depleted by decay and propagation effects. This explains why neutrinos dominate at low E_k, whereas the surviving muon component becomes dominant at higher E_k.

Another feature is the muon-neutrino spectra are higher than the electron-neutrino spectra. This is also consistent with conventional atmospheric decay chain described in the theoretical background. Muon-neutrinos are produced directly in charged-pion and charged-kaon decays, whereas electron-neutrinos are produced mainly through the subsequent muon decay. At higher energies, however, muons are more likely to reach the observation level before decaying, this reduces the electron-neutrino contribution. The $\nu_e + \bar{\nu}_e$ spectrum is therefore lower and falls more steeply than the $\nu_\mu + \bar{\nu}_\mu$ spectrum.

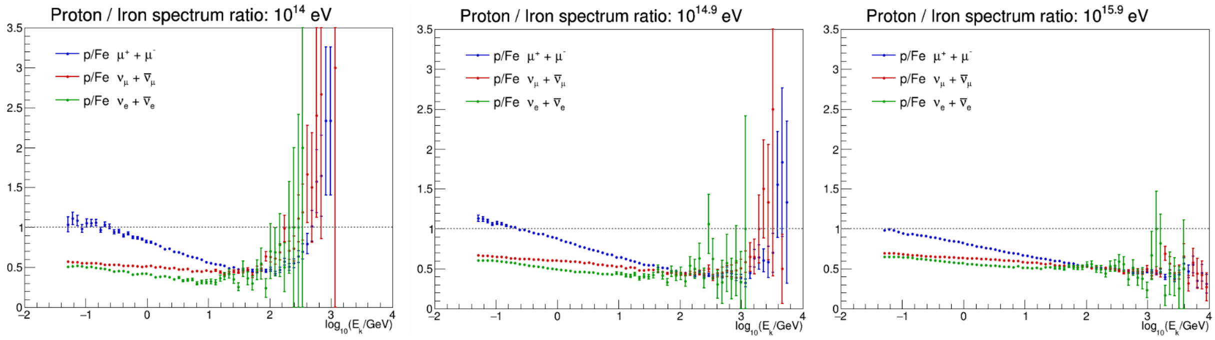

Figure A.2: Proton-to-iron ratios of the average kinetic-energy spectra of conventional muons, muon-neutrinos and electron-neutrinos at IceCube observation level for primary energies 10^{14}, $10^{14.9}$, and $10^{15.9}$ eV. The dashed horizontal line marks $R_{p/Fe} = 1$, where proton and iron showers produce the same average yield. Values below unity indicate larger yields from iron showers, while values above unity indicate larger yields from proton showers. The large fluctuations at the highest secondary energies are caused by limited particle statistics in the sparsely populated tail of the spectra.

The comparison between proton and iron showers shows the role of primary mass. At the same total primary energy, an iron nucleus can be approximated as a superposition of $A = 56$ nucleons, each with energy E_0/A following the superposition model (Gaisser et al., 2016). Iron showers therefore tend to interact earlier in the atmosphere and produce a larger number of lower-energy secondaries, while proton showers have a larger energy per participating nucleon and can produce a harder high-energy secondaries tail. This behaviour is reflected in **Figure A.1** and is quantified in **Figure A.2**, where the ratio

$$R_{p/Fe}(E_k) = \frac{(1/N_{\text{showers}})\mathrm{d}N_p/d\log_{10}(E_k/\mathrm{GeV})}{(1/N_{\text{showers}})\mathrm{d}N_{Fe}/d\log_{10}(E_k/\mathrm{GeV})} \tag{A.17}$$

with the error

$$\frac{\Delta R}{R} = \sqrt{\left(\frac{\Delta N_p}{N_p}\right)^2 + \left(\frac{\Delta N_{Fe}}{N_{Fe}}\right)^2} \tag{A.18}$$

is plotted for muons, muon-neutrinos, and electron-neutrinos. Generally, the ratios remain below unity, meaning that iron showers produce a larger average yield of conventional leptons at the observation level. But, there is a notable feature, the low-energy end of the muon ratio is slightly above unity $R_{p/Fe} > 1$. This means that, in the lowest observed muon-energy bins, proton showers produce more muons at the observation level than iron showers. This feature has been observed and interpreted in the work by Hector Ortiz et al. (Ortiz et al., 2023). In this work, they studied the muon number of the primary energies around 1 TeV at the detector level of 4800 m altitude. They showed that proton-induced showers can deposit more muons than iron-induced showers because many low-energy iron-shower muons decay before reaching detector level, since iron showers develop earlier in the atmosphere than proton showers. The same trend appears in the present simulations. However, in this thesis, the primary energies are much higher, $E_{\text{prim}} > 100$ TeV, and the observation level is at 2840 m, so this feature would need further statistics to confirm this interpretation quantitatively. The apparent rise and large error bar of the ratios at the highest secondary energies is due to statistical limitation and would not be considered for interpretation.

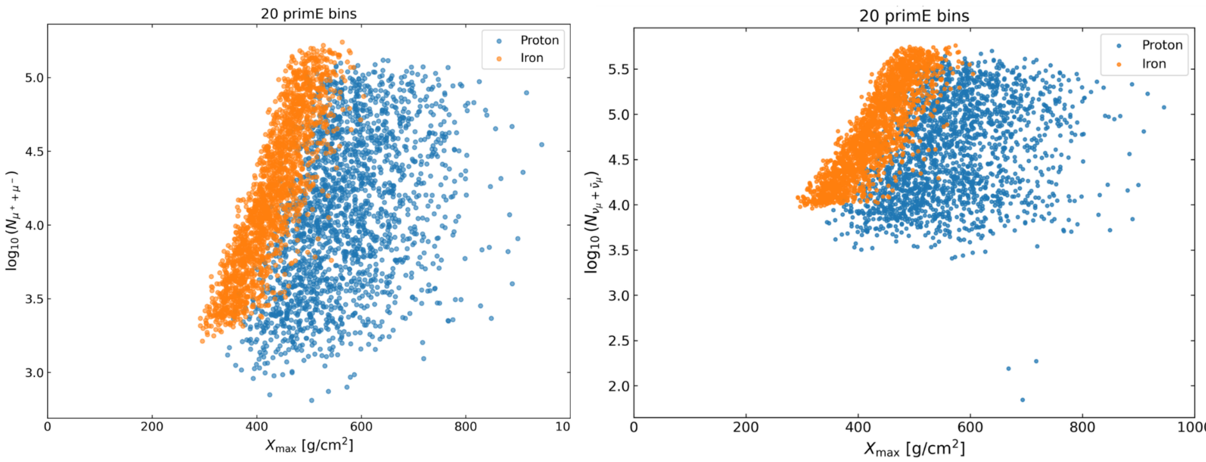

Figure A.3: Shower-by-shower dependence of the total muon and muon-neutrino multiplicities on the depth of shower maximum, $X_{\max}$, for proton- and iron-induced CORSIKA showers across 20 primary-energy bins. The left panel shows $\log_{10}(N_{\mu^+ + \mu^-})$ at $X_{\max}$, while the right panel shows $\log_{10}(N_{\nu_\mu + \bar{\nu}_\mu})$. Proton showers populate a broader and generally deeper $X_{\max}$ range, whereas iron showers are concentrated at smaller $X_{\max}$, reflecting the earlier development and smaller shower-to-shower fluctuations of heavy primaries.

The behaviour of primary masses is confirmed and further demonstrated in **Figure A.3**. The quantity $X_{\max}$ is the atmospheric depth at which a shower reaches its maximum development. The superposition model (Gaisser et al., 2016) describes that the maximum development of a shower is sensitive to its primary mass, since heavier nuclei has more nucleon thus can interact earlier and develop higher in the atmosphere.

In both panels, proton showers span a broader maximum-depth range and extend to larger depths, whereas iron showers form a narrower population at the smaller depth. This broader proton distribution reflects the larger intrinsic shower-to-shower fluctuations of proton-induced showers, which arise primarily from the larger fluctuations in the depth of the first interaction.

Since the present figure combines many primary energy bins, the observed trends reflect both energy and mass effects. A quantitative interpretation of $X_{\max}$ dependence would require the same analysis in fixed primary-energy bins. In this section, the **Figure A.3** is used mainly to show the global separation between proton and iron shower development and to support the interpretation of the spectral and ratio results.

A.3.2 Primary-Energy Dependence

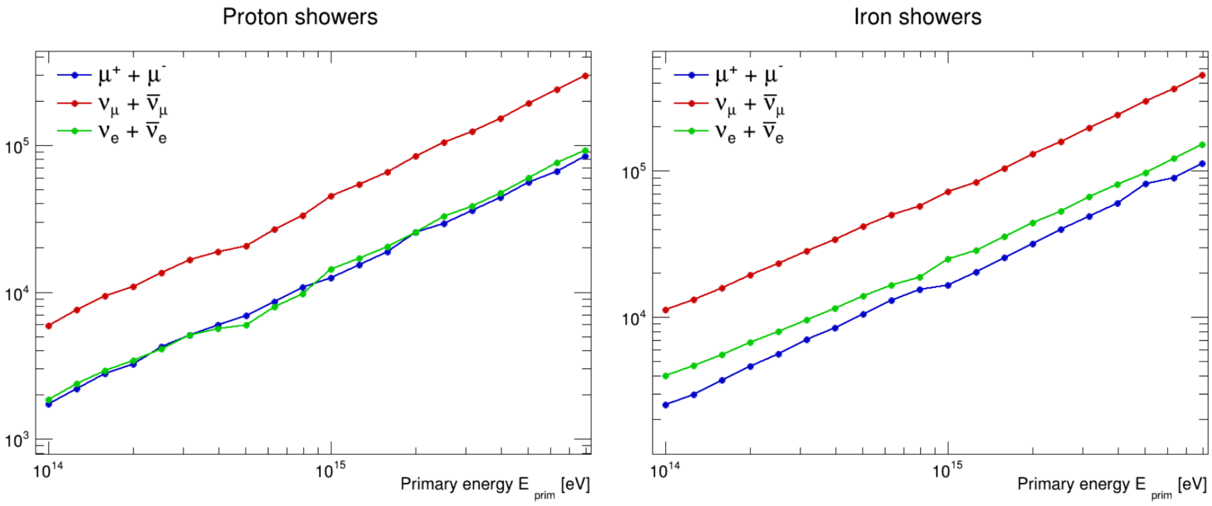

Figure A.4: Mean total Number of conventional muons, muon-neutrinos, and electron-neutrinos per shower against primary energy for CORSIKA proton- and iron-induced air showers. The left panel shows proton primaries and the right panel shows iron primaries across 20 primary-energy bins. The yields increase monotonically with E_{prim}, reflecting the larger secondary-particle multiplicity in higher-energy hadronic cascades. Muon-neutrinos form the largest component in both primary samples, while iron showers produce larger total lepton yields than proton showers at the same primary energy.

The **Figure A.4** shows the total particle multiplicity at the observation level for each of the 20 primary-energy bins.

The first clear feature is that all three particle yields increase monotonically with primary energy for both proton and iron primaries. On the logarithmic axes, the trends are close to linear, indicating an approximately power-law dependence of the form

$$\langle N_i \rangle \propto E_{\text{prim}}^{\alpha_i}, \tag{A.19}$$

where $i = \mu^\pm, \nu_\mu + \bar{\nu}_\mu, \nu_e + \bar{\nu}_e$. This is expected from hadronic cascade physics, where a higher-energy primary produces more secondary pions and kaons, which then either interact again or decay into muons and neutrinos. The cascade equations in the theoretical background describe this behaviour through gain terms from parent-particle interactions and decays, so increasing the primary energy increases the total energy available for secondary-particle production.

The muon-neutrino yield is the largest component over the full primary-energy range for both proton and iron showers. This hierarchy follows from the conventional decay chain. Muon-neutrinos are produced directly in charged-pion and charged-kaon decays, and are also produced again in subsequent muon decay. Electron-neutrinos, in contrast, are produced mainly through muon decay. Therefore, when the full pion- and muon-decay chain develops, the production number of muon-neutrinos is expected to exceed the number of electron-neutrinos. **Figure A.4** also shows that, we can see the ratio $(\nu_\mu + \bar{\nu}_\mu)/(\nu_e + \bar{\nu}_e)$ exceed 2. This is consistent with the approximate relation of muon-neutrino and electron-neutrino at high energies, when muons reach the observation level before decaying due to relativistic effect.

Comparing the two panels, we can see that the iron shower gives larger total yields of both muons and neutrinos than the proton shower. We can also see the difference in the ordering of the muon and electron-neutrino curves. The $\mu^+ + \mu^-$ and $\nu_e + \bar{\nu}_e$ yields are very close in the proton case, while in the iron case, the electron-neutrino yield is significantly above the muon yield. These features are, again, demonstrate for the different behaviour of the primary masses following the superposition model (Gaisser et al., 2016). Iron showers develop earlier in the atmosphere and therefore produce a larger fraction of low-energy secondary mesons and muons at higher altitude. Therefore, a larger fraction of these lower-energy muons can decay before reaching the observation level. This increasing the electron-neutrino yield while reducing the surviving muon count, as shown in the **Figure A.4**.

A.3.3 Zenith-Angle Dependence

The zenith-angle dependence of the simulated lepton yields is presented using two complementary representations: the total number of particles per shower as a function of zenith angle, and the corresponding spectra coloured by zenith angle. The total-yield curves give the global angular trend, while the spectra show which secondary-energy regions have the strongest zenith-angle dependence. In all cases, CORSIKA results are compared with MCEq predictions to check whether the shower-by-shower MC simulation follows the expected average cascade behaviour.

The angular behaviour differs between muons and neutrinos because they respond differently to the increased slant depth of inclined showers. For muons (**Figure A.5**), the total yield is approximately constant at small and intermediate zenith angles, but decreases at larger zenith angles, especially above $\theta \approx 40°$. This is most visible in the muon total-yield curves and is physically expected: inclined showers have longer atmospheric paths, so low-energy muons have more time to decay or lose energy by ionisation before reaching the observation level. The energy-resolved muon spectra (**Figure A.6**) confirm that this is not a uniform suppression across all energies. The low- and intermediate-energy parts of the muon spectrum are most sensitive to zenith angle, whereas the high-energy muon component is more stable because relativistic time dilation increases the muon survival probability.

The electron-neutrino component shows the opposite tendency (**Figure A.7**). The total $\nu_e + \bar{\nu}_e$ yield generally increases with zenith angle over the simulated angular range, and the spectra show an enhancement over the populated low- and intermediate-energy region. This follows from the conventional decay chain where electron neutrinos are mainly produced through muon decay. A longer inclined path increases the probability that secondary muons decay before reaching the observation level. Therefore, the same propagation effect that reduces the surviving low-energy muon population can increase the electron-neutrino yield.

The muon-neutrino component show a less dependence on zenith angles (**Figure A.9**). Its total yield is less strongly suppressed than the muon yield and less clearly enhanced than the electron-neutrino yield. This is because $\nu_\mu + \bar{\nu}_\mu$ was produced in both charged-pion, charged-kaon decays and muon decay. These effects partially compensate each other, so the muon-neutrino yield remains comparatively stable with zenith angle.

The CORSIKA and MCEq results show the same broad angular behaviour. MCEq gives smooth inclusive cascade predictions, while CORSIKA shows statistical fluctuations from finite shower samples. The agreement is generally good, especially for muon yields, in the good statistics regions of the spectra and in the total-yield trends. Larger deviations occur mainly in sparsely populated high-energy tails, where the number of CORSIKA particles is small and statistical uncertainty is larger.

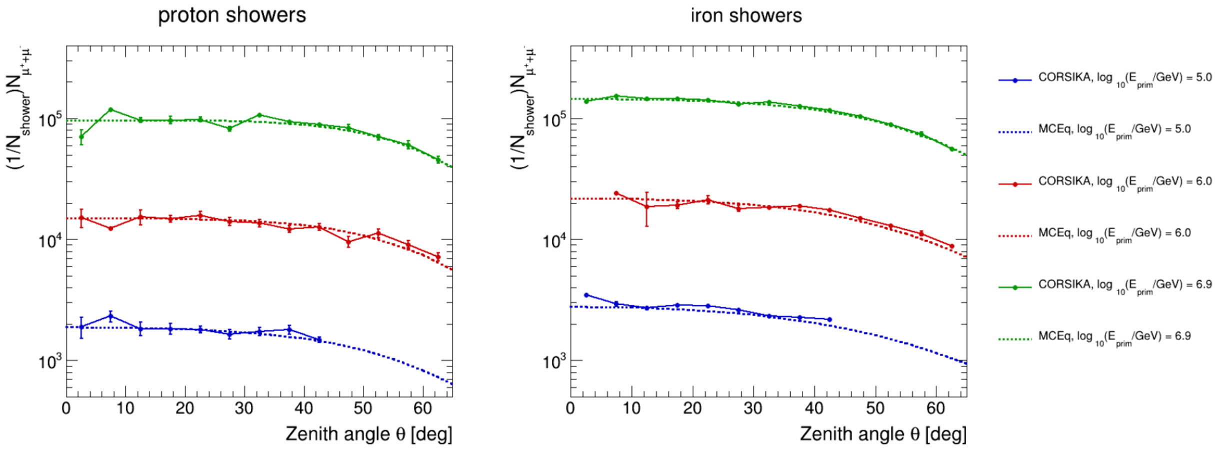

Figure A.5: Zenith-angle dependence of the mean total number of conventional muons per shower for proton- and iron-induced CORSIKA air showers. The left panel shows proton primaries and the right panel shows iron primaries for primary-energy bins: $E_{\text{prim}} = 10^5$, 10^6, and $10^{6.9}$ GeV. Solid points show the CORSIKA mean with statistical uncertainties, while dotted curves show the corresponding MCEq predictions. The decrease at large zenith angles reflects the longer atmospheric path length and the increased probability of muon decay or energy loss before reaching the observation level.

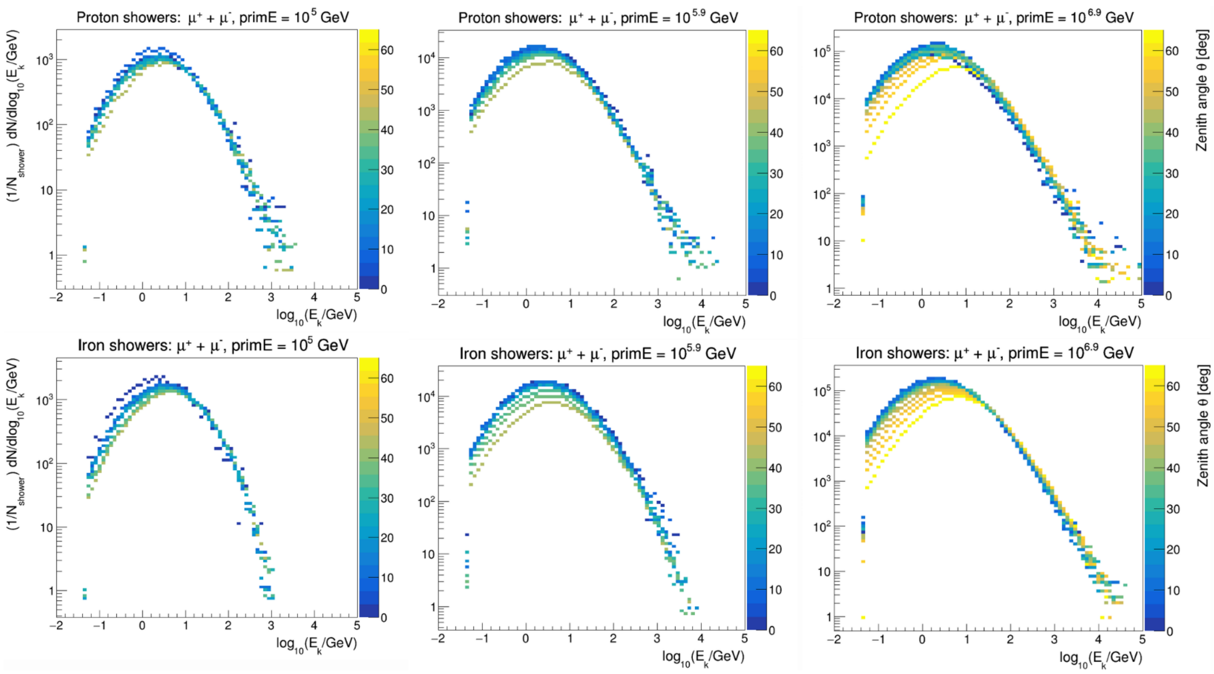

Figure A.6: Zenith-angle dependence of the conventional muon spectra for proton- and iron-induced CORSIKA air showers. The upper row shows proton primaries and the lower row shows iron primaries. The columns correspond to $E_{\text{prim}} = 10^5$, 10^6, and $10^{6.9}$ GeV. The colour scale indicates the zenith angle θ. The angular dependence is strongest in the low- and intermediate-energy muon population, where decay and energy-loss effects during propagation are most important.

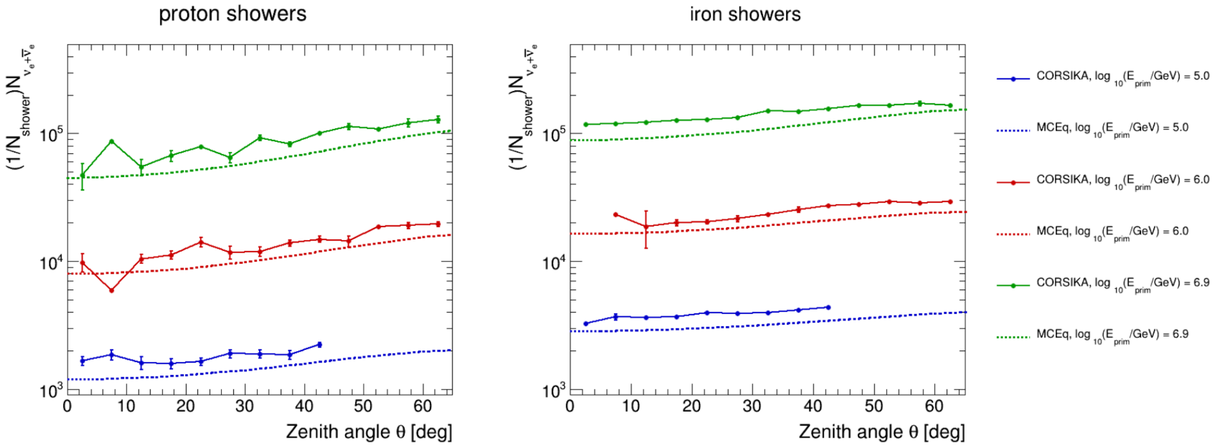

Figure A.7: Zenith-angle dependence of the mean total number of conventional electron-neutrinos and antineutrinos per shower for proton- and iron-induced CORSIKA air showers. The left panel shows proton primaries and the right panel shows iron primaries for primary-energy bins: $E_{\text{prim}} = 10^5$, 10^6, and $10^{6.9}$ GeV. Solid points show the CORSIKA mean with statistical uncertainties, while dotted curves show the corresponding MCEq predictions. The generally increasing trend with zenith angle indicates enhanced electron-neutrino production from muon decay along longer atmospheric slant paths.

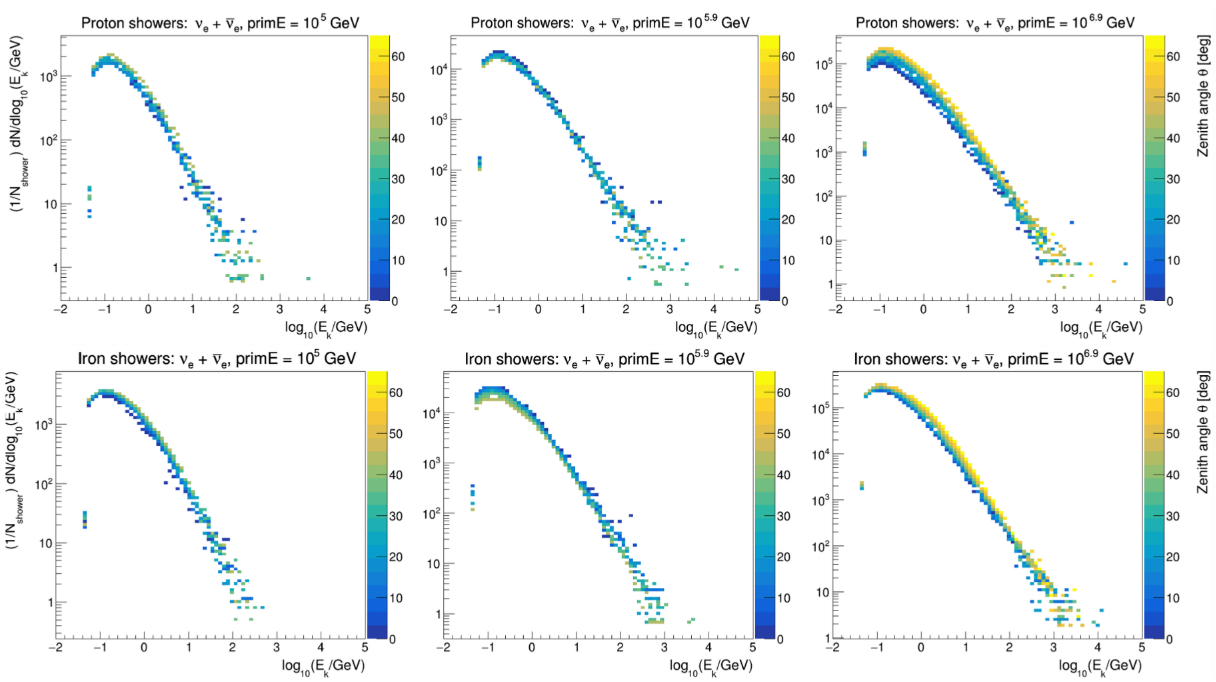

Figure A.8: Zenith-angle dependence of the conventional electron-neutrino spectra for proton- and iron-induced CORSIKA air showers. The upper row shows proton primaries and the lower row shows iron primaries. The columns correspond to $E_{\text{prim}} = 10^5$, 10^6, and $10^{6.9}$ GeV. The colour scale indicates the zenith angle θ. The enhancement at larger zenith angles reflects the increased probability of muon decay along longer atmospheric paths, which feeds the $\nu_e + \bar{\nu}_e$ component.

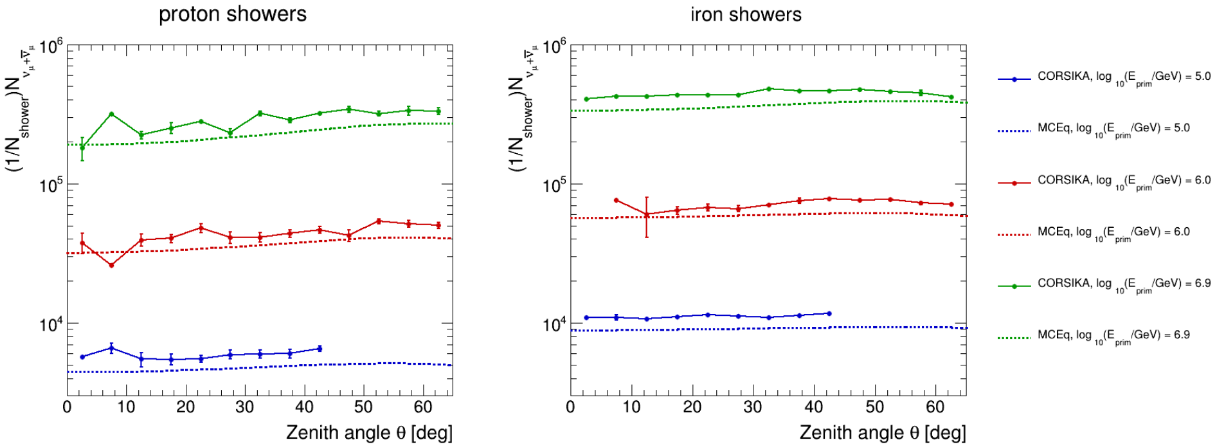

Figure A.9: Zenith-angle dependence of the mean total number of conventional muon-neutrinos and antineutrinos per shower for proton- and iron-induced CORSIKA air showers. The left panel shows proton primaries and the right panel shows iron primaries for primary-energy bins: $E_{\text{prim}} = 10^5$, 10^6, and $10^{6.9}$ GeV. Solid points show the CORSIKA mean with statistical uncertainties, while dotted curves show the corresponding MCEq predictions. The muon-neutrino yield is less strongly suppressed with zenith angle than the muon yield because $\nu_\mu + \bar{\nu}_\mu$ receives contributions from both direct meson decay and subsequent muon decay.

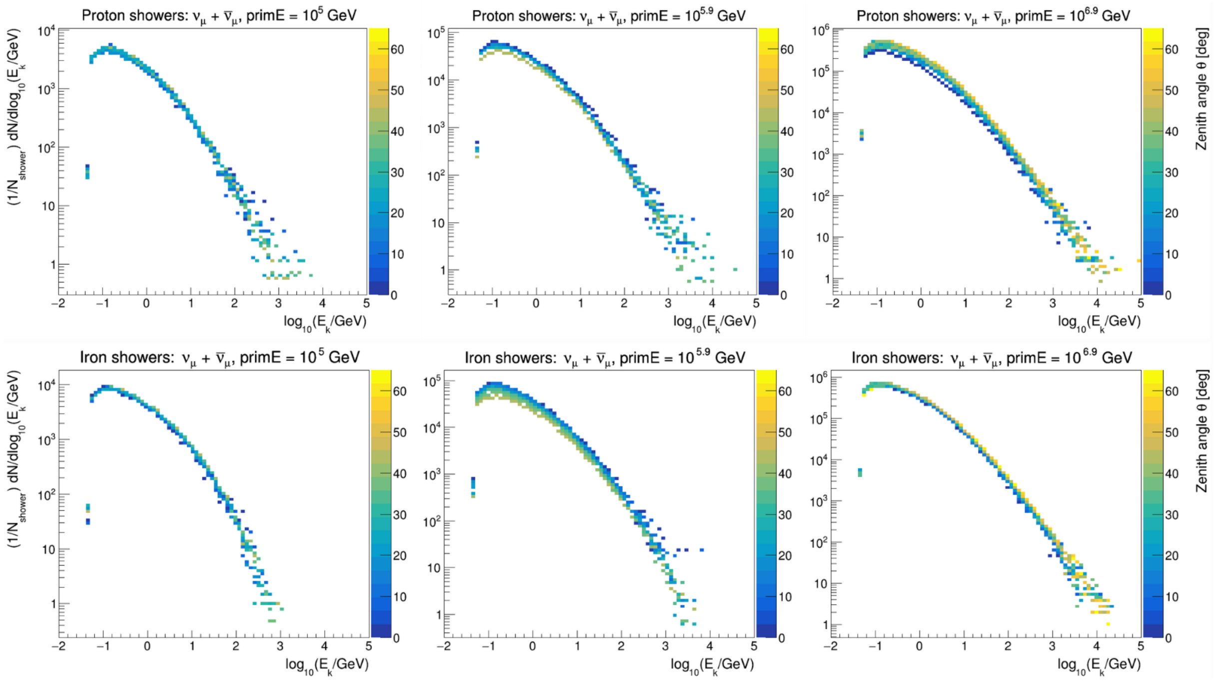

Figure A.10: Zenith-angle dependence of the conventional muon-neutrino spectra for proton- and iron-induced CORSIKA air showers. The upper row shows proton primaries and the lower row shows iron primaries. The columns correspond to $E_{\text{prim}} = 10^5$, 10^6, and $10^{6.9}$ GeV. The colour scale indicates the zenith angle θ. The spectra plot shows relatively weak dependence of muon-neutrino production with zenith angles.